Effective-one-body waveforms calibrated to numerical relativity simulations: Coalescence of nonspinning, equal-mass black holes

Alessandra Buonanno,[1] Yi Pan,[1] Harald P. Pfeiffer,[2] Mark A. Scheel,[2] Luisa T. Buchman,[2] and Lawrence E. Kidder[3]
[1]*Maryland Center for Fundamental Physics, Department of Physics, University of Maryland, College Park, Maryland 20742, USA*
[2]*Theoretical Astrophysics 130-33, California Institute of Technology, Pasadena, California 91125, USA*
[3]*Center for Radiophysics and Space Research, Cornell University, Ithaca, New York, 14853*
(Received 4 February 2009; published 17 June 2009)

We calibrate the effective-one-body (EOB) model to an accurate numerical simulation of an equal-mass, nonspinning binary black-hole coalescence produced by the Caltech-Cornell Collaboration. Aligning the EOB and numerical waveforms at low frequency over a time interval of $\sim 1000M$, and taking into account the uncertainties in the numerical simulation, we investigate the significance and degeneracy of the EOB-adjustable parameters during inspiral, plunge, and merger, and determine the minimum number of EOB-adjustable parameters that achieves phase and amplitude agreements on the order of the numerical error. We find that phase and fractional amplitude differences between the numerical and EOB values of the dominant gravitational-wave mode h_{22} can be reduced to 0.02 radians and 2%, respectively, until a time $20M$ before merger, and to 0.04 radians and 7%, respectively, at a time $20M$ after merger (during ringdown). Using LIGO, Enhanced LIGO, and Advanced LIGO noise curves, we find that the overlap between the EOB and the numerical h_{22}, maximized only over the initial phase and time of arrival, is larger than 0.999 for equal-mass binary black holes with total mass 30–$150M_{\odot}$. In addition to the leading gravitational mode (2, 2), we compare the dominant subleading modes (4, 4) and (3, 2) for the inspiral and find phase and amplitude differences on the order of the numerical error. We also determine the mass-ratio dependence of one of the EOB-adjustable parameters by calibrating to numerical *inspiral* waveforms for black-hole binaries with mass ratios 2:1 and 3:1. The results presented in this paper improve and extend recent successful attempts aimed at providing gravitational-wave data analysts the best analytical EOB model capable of interpolating accurate numerical simulations.

DOI: 10.1103/PhysRevD.79.124028 PACS numbers: 04.25.D−, 04.25.dg, 04.25.Nx, 04.30.−w

I. INTRODUCTION

The first-generation gravitational-wave detectors—the Laser Interferometer Gravitational Wave Observatory (LIGO) [1,2], GEO [3], and Virgo [4]—have operated at design sensitivity for a few years, providing new upper limits for several astrophysical sources. They are now undergoing an upgrade to Enhanced LIGO and Virgo^{+}; this will improve their sensitivity by a factor of ~ 2. The second-generation interferometers, Advanced LIGO [5], and Advanced Virgo, will start operating in 2013–2015 with an overall improvement in sensitivity by a factor of ~ 10, thus increasing the event rates for many astrophysical sources by a factor of 1000.

One of the most promising sources for these detectors is the inspiral and merger of compact binary systems of black holes (BHs). The search for gravitational waves (GWs) from coalescing binaries and the extraction of parameters are based on the matched-filtering technique [6,7], which requires a rather accurate knowledge of the waveform of the incoming signal [8]. In particular, the detection and subsequent data analysis of GW signals are made by using a bank of templates modeling the GWs emitted by the source.

The effective-one-body (EOB) formalism was introduced [9,10] as a promising approach to describe analytically the inspiral, merger, and ringdown waveforms emitted during a binary merger. Necessary inputs for the EOB approach include high-order post-Newtonian (PN) results [11] for two-body conservative dynamics, radiation-reaction force, and gravitational waveforms. For compact bodies, the PN approximation is essentially an expansion in the characteristic orbital velocity v/c or, equivalently, in the gravitational potential, $GM/(rc^2)$, with r the typical separation and M the total binary mass. The EOB approach, however, does not use the PN results in their original *Taylor-expanded* forms (i.e., as polynomials in v/c), but instead in some *resummed* forms [9,10,12–17]. The latter are designed to incorporate some of the expected nonperturbative features of the exact results.

As it is now possible to produce very accurate numerical simulations of comparable mass binary black-hole coalescences (see e.g., [18–25]), we can compare in detail the EOB predictions with numerical results, and when necessary, introduce new features into the EOB model in order to improve its agreement with the numerical results. This is an important avenue to LIGO, GEO, and Virgo template construction, as eventually thousands of waveform templates may be needed to detect the GW signal within the detector noise, and to extract astrophysical information from the observed waveform. Given the high computational cost of running the numerical simulations, template

construction is currently an impossible demand for numerical relativity alone.

This paper builds upon a rather successful recent effort [22,26–31] aimed at producing the best analytical EOB model able to interpolate accurate numerical simulations. Other approaches based on phenomenological waveforms have also been proposed [32,33]. Here, we calibrate the EOB model to the most accurate numerical simulation to date of an equal-mass, nonspinning binary black-hole merger that has been produced with a pseudospectral code by the Caltech-Cornell Collaboration [21,23]. Taking into account the uncertainties in the numerical simulation, we investigate the significance and degeneracy of the EOB-adjustable parameters and determine the minimal number of adjustable parameters that achieves as good agreement as possible between the numerical and EOB GW's phase and amplitude. In addition to the leading GW mode $(\ell, m) = (2, 2)$, we also compare the leading subdominant modes (4, 4) and (3, 2). By reducing the phase difference between the EOB and numerical *inspiral* waveforms of black-hole binaries with mass ratios $q = m_1{:}m_2$ of 2:1 and 3:1, we explore the dependence of one of the adjustable parameters on the symmetric mass ratio $\nu = m_1 m_2/(m_1 + m_2)^2$.

The paper is organized as follows: In Sec. II, we briefly review the EOB dynamics and waveforms. In Sec. III, we calibrate the EOB model to the numerical simulation of an equal-mass nonspinning binary black-hole coalescence and determine the region of the parameter space of the EOB-adjustable parameters that leads to the best agreement with the numerical results. We also discuss the impact of our results on data analysis, and calibrate the EOB model with inspiral waveforms from accurate numerical simulations of nonspinning black-hole binaries with mass ratios 2:1 and 3:1. Section IV summarizes our main conclusions. Finally, the Appendix compares the numerical $h_{\ell m}$ extracted with the Regge-Wheeler-Zerilli (RWZ) formalism with the $h_{\ell m}$ obtained by two time integrals of the Newman-Penrose (NP) scalar $\Psi_4^{\ell m}$.

II. EFFECTIVE-ONE-BODY MODEL

In this section, we briefly review the EOB dynamics and waveforms, focusing mainly on the adjustable parameters. More details can be found in Refs. [9,10,13,15,22,26,28–31]. Here, we follow Refs. [22,28].

A. Effective-one-body dynamics

We set $M = m_1 + m_2$, $\mu = m_1 m_2/M = \nu M$, and use natural units $G = c = 1$. In absence of spins, the motion is constrained to a plane. Introducing polar coordinates (r, Φ) and their conjugate momenta (p_r, p_Φ), the EOB effective metric takes the form [9]

$$ds^2_{\rm eff} = -A(r)dt^2 + \frac{D(r)}{A(r)}dr^2 + r^2(d\theta^2 + \sin^2\theta d\Phi^2). \quad (1)$$

Following Refs. [16,34], we replace the radial momentum p_r with p_{r_*}, the conjugate momentum to the EOB *tortoise* radial coordinate r_*:

$$\frac{dr_*}{dr} = \frac{\sqrt{D(r)}}{A(r)}. \quad (2)$$

In terms of p_{r_*} the nonspinning EOB Hamiltonian is [9]

$$H^{\rm real}(r, p_{r*}, p_\Phi) \equiv \mu \hat{H}^{\rm real} = M\sqrt{1 + 2\nu\left(\frac{H_{\rm eff} - \mu}{\mu}\right)} - M, \quad (3)$$

with the effective Hamiltonian [9,13,34]

$$H^{\rm eff}(r, p_{r*}, p_\Phi) \equiv \mu \hat{H}^{\rm eff} = \mu\sqrt{p^2_{r*} + A(r)\left[1 + \frac{p^2_\Phi}{r^2} + 2(4 - 3\nu)\nu\frac{p^4_{r*}}{r^2}\right]}. \quad (4)$$

The Taylor approximants to the coefficients $A(r)$ and $D(r)$ can be written as [9,13]

$$A_k(r) = \sum_{i=0}^{k+1} \frac{a_i(\nu)}{r^i}, \quad (5)$$

$$D_k(r) = \sum_{i=0}^{k} \frac{d_i(\nu)}{r^i}. \quad (6)$$

The functions $A(r)$, $D(r)$, $A_k(r)$, and $D_k(r)$ all depend on the symmetric mass ratio ν through the ν-dependent coefficients $a_i(\nu)$ and $d_i(\nu)$. These coefficients are currently known through 3PN order (i.e., up to $k = 4$) and can be read from Eqs. (47) and (48) in Ref. [22]. Previous investigations [15,22,28–31] have demonstrated that, during the last stages of inspiral and plunge, the EOB dynamics can be adjusted closer to the numerical simulations by including in the radial potential $A(r)$ a pseudo 4PN (p4PN) coefficient $a_5(\nu)$. This coefficient has so far been treated as a *linear* function in ν, i.e., $a_5(\nu) = \lambda_0\nu$, with λ_0 a constant.[1] In this paper, however, we shall also explore the possibility of going beyond this linear dependence, such that

$$a_5(\nu) = \nu(\lambda_0 + \lambda_1\nu), \quad (7)$$

where λ_0 and λ_1 are constants. In order to assure the presence of a horizon in the effective metric (1), a zero needs to be factored out from $A(r)$. This is obtained by applying a Padé resummation [13]. The Padé coefficients for the expansion of $A(r)$ and $D(r)$ at p4PN order are denoted $A^1_4(r)$ and $D^0_4(r)$, and their explicit form can be read from Eqs. (54) and (59) in Ref. [22].

[1]Note that λ_0 was denoted λ in Ref. [28], and a_5 in Refs. [22,29–31].

The EOB Hamilton equations are written in terms of the reduced (i.e., dimensionless) quantities $\hat{H}^{\rm real}$ [defined in Eq. (3)], $\hat{t} = t/M$, and $\hat{\Omega} = \Omega M$ [10]:

$$\frac{dr}{d\hat{t}} = \frac{A(r)}{\sqrt{D(r)}} \frac{\partial \hat{H}^{\rm real}}{\partial p_{r_*}}(r, p_{r_*}, p_\Phi), \tag{8}$$

$$\frac{d\Phi}{d\hat{t}} = \frac{\partial \hat{H}^{\rm real}}{\partial p_\Phi}(r, p_{r_*}, p_\Phi), \tag{9}$$

$$\frac{dp_{r_*}}{d\hat{t}} = \frac{A(r)}{\sqrt{D(r)}}\left[-\frac{\partial \hat{H}^{\rm real}}{\partial r}(r, p_{r_*}, p_\Phi) + \hat{\mathcal{F}}_r(r, p_{r_*}, p_\Phi)\right], \tag{10}$$

$$\frac{dp_\Phi}{d\hat{t}} = \hat{\mathcal{F}}_\Phi(r, p_{r_*}, p_\Phi), \tag{11}$$

with the definition $\hat{\Omega} \equiv d\Phi/d\hat{t}$. Furthermore, for the Φ component of the radiation-reaction force we use the non-Keplerian Padé approximant to the energy flux [12,35]

$$\hat{\mathcal{F}}_\Phi = {}^{\rm nK}\hat{\mathcal{F}}_4^4 \equiv -\frac{v_\Omega^3}{\nu V_\Phi^6} F_4^4(V_\Phi; \nu, v_{\rm pole}), \tag{12}$$

where $v_\Omega \equiv \hat{\Omega}^{1/3}$, $V_\Phi \equiv \hat{\Omega} r_\Omega$, and $r_\Omega \equiv r[\psi(r, p_\Phi)]^{1/3}$. Here, ψ is defined by Eqs. (66)–(68) of Ref. [22]. As the EOB Hamiltonian is a deformation of the Schwarzschild Hamiltonian, the exact Keplerian relation $\hat{\Omega}^2 r_\Omega^3 = 1$ holds. The quantity F_4^4 in Eq. (12) is given by Eqs. (39) and (40) in Ref. [22],[2] and it uses the Taylor-expanded energy flux (as given by Eq. (19) in Ref. [22]) in the form

$$\begin{aligned}\mathcal{F}_8(\nu) = &-\frac{323\,105\,549\,467}{3\,178\,375\,200} + \frac{232\,597}{4410}\gamma_E - \frac{1369}{126}\pi^2 \\ &+ \frac{39\,931}{294}\log 2 - \frac{47\,385}{1568}\log 3 \\ &+ \frac{232\,597}{4410}\log v_\Omega + \nu A_8,\end{aligned} \tag{13}$$

where we combine the known test-mass-limit terms [36] with a p4PN adjustable parameter A_8 [22].[3]

The radial component of the radiation-reaction force $\hat{\mathcal{F}}_r(r, p_{r_*}, p_\Phi)$ in Eq. (10) was neglected in previous studies [22,26,28–31] because Ref. [10] showed that for quasicircular motion, in some gauges, it can be set to zero. Furthermore, it was shown in Ref. [10] that if the motion remains quasicircular even during the plunge, $\hat{\mathcal{F}}_r(r, p_{r_*}, p_\Phi)$ does not affect the dynamics considerably. However, since we are trying to capture effects in the numerical simulations that go beyond the quasicircular motion assumption, we find it interesting to add $\hat{\mathcal{F}}_r(r, p_{r_*}, p_\Phi)$ [see Eq. (3.18) of Ref. [10] and the discussion around it]. We set

$$\hat{\mathcal{F}}_r(r, p_{r_*}, p_\Phi) = a_{\rm RR}^{\mathcal{F}_r}(\nu)\frac{\dot{r}}{r^2\Omega}\hat{\mathcal{F}}_\Phi(r, p_{r_*}, p_\Phi), \tag{14}$$

where $a_{\rm RR}^{\mathcal{F}_r}(\nu)$ is an adjustable parameter.

Finally, the tangential force described by Eq. (12) applies only to quasicircular motion. This tangential force could also in principle contain terms describing the departure from quasicircular motion during the last stages of inspiral and plunge. There are several ways to include such non-quasicircular (NQC) terms [15,22,31]; here we do so by replacing the quantity $\hat{\mathcal{F}}_\Phi$ on the right-hand side of Eq. (11) [but not the $\hat{\mathcal{F}}_\Phi$ on the right-hand side of Eq. (14)] with ${}^{\rm NQC}\hat{\mathcal{F}}_\Phi$, where

$${}^{\rm NQC}\hat{\mathcal{F}}_\Phi \equiv \hat{\mathcal{F}}_\Phi\left(1 + a_{\rm RR}^{\mathcal{F}_\Phi}(\nu)\frac{\dot{r}^2}{(r\Omega)^2}\right), \tag{15}$$

and $a_{\rm RR}^{\mathcal{F}_\Phi}(\nu)$ is an additional adjustable parameter. The form of this NQC correction will be discussed further in Sec. III B. Note that alternative NQC terms have been proposed in the literature—for example, in Ref. [15] the authors used $p_r^2/(p_\Phi/r^2)$, while Ref. [31] employed $p_{r_*}^2/(r\Omega)^2$. In summary, in the notation of Ref. [22], the EOB model used here is ${}^{\rm nK}F_4^4/H_4$ with adjustable parameters $\{a_5(\nu), v_{\rm pole}(\nu), a_{\rm RR}^{\mathcal{F}_\Phi}(\nu), a_{\rm RR}^{\mathcal{F}_r}(\nu), A_8\}$.

B. EOB waveform: Inspiral and Plunge

Having the inspiral dynamics in hand, we need to compute the gravitational waveform $h_{\ell m}$. Reference [21] compared the numerically extracted gravitational waveform h_{22} to the PN result with amplitude expressed as a *Taylor* expansion [37,38]; even when expanded to 3PN order, the amplitude disagreed by about 1% at times several hundred M before merger. As previous investigations [29–31] have shown, more accurate agreement with the numerical h_{22} amplitude can be obtained by applying several resummations to the Taylor-expanded h_{22} amplitude. These resummations have recently been improved using results in the quasicircular test-particle limit [17]. We follow Ref. [17] and write the EOB modes $h_{\ell m}$ as

$$\hat{h}_{22}(t) = -\frac{8M}{R}\sqrt{\frac{\pi}{5}}\nu e^{-2i\Phi}V_\Phi^2 F_{22}, \tag{16a}$$

$$\hat{h}_{44}(t) = -\frac{64M}{9R}\sqrt{\frac{\pi}{7}}\nu(1-3\nu)e^{-4i\Phi}V_\Phi^4 F_{44}, \tag{16b}$$

$$\hat{h}_{32}(t) = -\frac{8M}{3R}\sqrt{\frac{\pi}{7}}\nu(1-3\nu)e^{-2i\Phi}V_\Phi^4 F_{32}, \tag{16c}$$

[2]Note that here we use the Padé approximants with factorized logarithms, as originally proposed in Ref. [12], but we set $v_{\rm LSO} = 1$, so that the GW energy flux depends only on the two adjustable parameters $v_{\rm pole}$ and A_8.

[3]Note that in Ref. [22] the p4PN contribution in the GW energy flux also included the term $\nu B_8 \log v_\Omega$. Since we found appreciable degeneracy between A_8 and B_8, we disregard B_8, i.e., we set $B_8 = 0$.

where R is the luminosity distance from the binary, and with

$$F_{lm} = \begin{cases} \hat{H}_{\rm eff} T_{\ell m} (\rho_{\ell m})^{\ell} e^{i\delta_{\ell m}} & (\ell + m \text{ even}) \\ \hat{J}_{\rm eff} T_{\ell m} (\rho^{J}_{\ell m})^{\ell} e^{i\delta_{\ell m}} & (\ell + m \text{ odd}) \end{cases}, \tag{17}$$

where $\hat{H}_{\rm eff}$ and $\hat{J}_{\rm eff}$ are effective sources that in the test-particle, circular-motion limit contain a pole at the EOB light ring (photon orbit); here, $\hat{H}_{\rm eff}$ is given in Eq. (4), and $\hat{J}_{\rm eff} = p_{\Phi} v_{\Omega}$ is equal to the orbital angular momentum p_{Φ} normalized to the circular-orbit Newtonian angular momentum v_{Ω}^{-1}. The quantities $T_{\ell m}$, $\delta_{\ell m}$, $\rho_{\ell m}$, $\rho^{J}_{\ell m}$ can be read from Eqs. (19), (20), (23), (25), (C1), (C4) and (C6) in Ref. [17], respectively. More specifically, $T_{\ell m}$ is a resummed version [16] of an infinite number of leading logarithms entering the tail effects; $\delta_{\ell m}$ is a supplementary phase [16], which corrects the phase effects not included in the complex tail factor; $\rho_{\ell m}$ and $\rho^{J}_{\ell m}$ are the resummed expressions of higher-order PN effects as recently proposed in Ref. [17] in the test-particle circular-orbit limit. The latter resummation was proposed to cure, among other effects, the linear growth with ℓ of the 1PN corrections in the Taylor-expanded amplitude.

Furthermore, motivated by the PN expansion for generic orbits, to include NQC effects in $h_{\ell m}$ we write

$$\begin{aligned} h^{\text{insp-plunge}}_{\ell m} &\equiv {}^{\rm NQC}h_{\ell m} \\ &= \hat{h}_{\ell m}\Bigg[1 + a_1^{h_{\ell m}} \frac{\dot{r}^2}{(r\Omega)^2} + \dot{r}^2\Bigg(a_2^{h_{\ell m}} \frac{\dot{r}^2}{(r\Omega)^2} \\ &\quad + a_3^{h_{\ell m}} \frac{M}{r} \frac{1}{(r\Omega)^2}\Bigg) + \dot{r}^4 a_4^{h_{\ell m}} \frac{M}{r} \frac{1}{(r\Omega)^2}\Bigg]. \end{aligned} \tag{18}$$

As we shall discuss in detail below, for the (2, 2) mode, one of the four adjustable parameters $a_i^{h_{22}}$ in Eq. (18) will be fixed by requiring that the peak of the EOB h_{22} occurs at the same time as the peak of the EOB orbital frequency [31] (i.e., at the EOB light ring); this requires no matching to a numerical waveform. Another of the $a_i^{h_{22}}$ will be fixed by requiring that the peak amplitude of the EOB and numerical waveforms agree. The final three $a_i^{h_{22}}$ parameters will be determined by minimizing the overall amplitude difference with respect to the numerical waveform. We note that an alternative NQC factor has been proposed in Ref. [31], notably $1 + a p_{r_*}^2/(\Omega^2 r^2 + \epsilon)$. We shall compare those different choices below.

C. EOB waveform: Merger and ringdown

The merger-ringdown waveform in the EOB approach is built as follows [10,26,28,30,31,35]: For each mode (ℓ, m) we write

$$h^{\text{merger-RD}}_{\ell m}(t) = \sum_{n=0}^{N-1} A_{\ell m n} e^{-i\sigma_{\ell m n}(t - t^{\ell m}_{\rm match})}, \tag{19}$$

where n is the overtone number of the Kerr quasinormal mode (QNM), N is the number of overtones included in our model, and $A_{\ell m n}$ are complex amplitudes to be determined by a matching procedure described below. The quantity $\sigma_{\ell m n} = \omega_{\ell m n} - i\alpha_{\ell m n}$, where the oscillation frequencies $\omega_{\ell m n} > 0$ and the inverse decay times $\alpha_{\ell m n} > 0$, are numbers associated with each QNM. The complex frequencies are known functions of the final black-hole mass and spin and can be found in Ref. [39]. The final black-hole masses and spins can be obtained from several fitting formulae to numerical results [28,34,40,41]. Here, we use the more accurate final black-hole mass and spin computed in Ref. [23]: $M_{\rm BH}/M = 0.95\,162 \pm 0.00\,002$, $a/M_{\rm BH} = 0.68646 \pm 0.00004$. While these numbers differ from the predictions of the fitting formulae in Ref. [28] by only 0.3%, such disagreement would be noticeable in our comparison. The matching time $t^{22}_{\rm match}(\nu)$ is an adjustable parameter that will be chosen to be very close to the EOB light ring [10] when matching the mode h_{22}.

The complex amplitudes $A_{\ell m n}$ in Eq. (19) are determined by matching the EOB merger-ringdown waveform with the EOB inspiral-plunge waveform. In order to do this, N independent complex equations are needed. In Refs. [10,26,28,35,42], the N equations were obtained at the matching time by imposing continuity of the waveform and its time derivatives

$$\begin{aligned} &\frac{d^k}{dt^k} h^{\text{insp-plunge}}_{\ell m}(t^{\ell m}_{\rm match}) = \frac{d^k}{dt^k} h^{\text{merger-RD}}_{\ell m}(t^{\ell m}_{\rm match}), \\ &\qquad (k = 0, 1, 2, \cdots, N-1), \end{aligned} \tag{20}$$

and we denote this approach *point matching*. In Refs. [30,31], the *comb matching* approach was introduced. In this approach, N equations are obtained at N points evenly sampled in a small time interval $\Delta t^{\ell m}_{\rm match}$ centered at $t^{\ell m}_{\rm match}$

$$\begin{aligned} &h^{\text{insp-plunge}}_{\ell m}\left(t^{\ell m}_{\rm match} + \frac{2k - N + 1}{2N - 2} \Delta t^{\ell m}_{\rm match}\right) \\ &= h^{\text{merger-RD}}_{\ell m}\left(t^{\ell m}_{\rm match} + \frac{2k - N + 1}{2N - 2} \Delta t^{\ell m}_{\rm match}\right), \\ &(k = 0, 1, 2, \cdots, N-1). \end{aligned} \tag{21}$$

Finally, the full (inspiral-plunge-merger-ringdown) EOB waveform reads

$$h_{\ell m} = h^{\text{insp-plunge}}_{\ell m} \theta(t^{\ell m}_{\rm match} - t) + h^{\text{merger-RD}}_{\ell m} \theta(t - t^{\ell m}_{\rm match}), \tag{22}$$

where $\theta(t)$ is the unit step function. The point matching approach gives better smoothness around the matching time, but it is not very stable numerically when N is large and higher-order numerical derivatives are needed. As we include eight QNMs in our ringdown waveforms, we find that the comb matching approach is more stable. To improve the smoothness of the comb matching we use here a *hybrid comb matching*: We choose a time interval $\Delta t^{\ell m}_{\rm match}$

ending at $t^{\ell m}_{\rm match}$, we impose the continuity of the waveform at $N-4$ points evenly sampled from $t^{\ell m}_{\rm match}-\Delta t^{\ell m}_{\rm match}$ to $t^{\ell m}_{\rm match}$, but we also require continuity of the first and second order time derivatives of the waveform at $t^{\ell m}_{\rm match}-\Delta t^{\ell m}_{\rm match}$ and $t^{\ell m}_{\rm match}$, thus guaranteeing the continuity of $\ddot{h}_{\ell m}$. Furthermore, we fix $t^{\ell m}_{\rm match}$ to be the time when the EOB orbital frequency reaches its maximum, and tune $\Delta t^{22}_{\rm match}$ in the range $2.5M$–$3.5M$ depending on the EOB dynamics.

It is worth noting that the lowest frequency among the eight QNMs included in our merger-ringdown waveform is $M\omega_{227}\sim 0.44$, which is larger than the EOB inspiral-plunge waveform frequency $M\omega(t^{22}_{\rm match})\sim 0.36$. Therefore, generically the EOB GW frequency will grow very rapidly from $M\omega\sim 0.36$ to $M\omega\sim 0.44$ immediately after the matching time, and this growth can be much more rapid than what is seen in the numerical simulation. We find that we can avoid this rapid growth by carefully fine-tuning the matching interval $\Delta t^{22}_{\rm match}$, and this is what we do for the comparisons presented here. Quite interestingly, we find that the h_{22} matching can be made much less sensitive to $\Delta t^{22}_{\rm match}$ if we include a pseudo QNM that has a frequency $M\omega(t^{22}_{\rm match})\sim 0.36$ and a decay time comparable to that of the highest overtone $\tau_{227}\sim 0.7M$. We refer to this QNM as pseudo because its frequency and decay time do not coincide with any of the QNMs of our final Kerr BH [39,43]. Although we do not use this pseudo QNM in the present analysis, we expect that its inclusion can help when matching higher modes of equal and unequal-mass binaries, and we shall consider it in the future.

III. CALIBRATING THE EFFECTIVE-ONE-BODY WAVEFORMS TO NUMERICAL RELATIVITY SIMULATIONS

We shall now calibrate the EOB model against a numerical simulation of an equal-mass nonspinning binary black hole. This simulation was presented as run ''30c1/N6'' in Scheel *et al.* [23], and the inspiral part of the waveform was used in previous comparisons with PN models [21,22]. In addition to the NP scalars $\Psi_4^{\ell m}$ extracted from this simulation, we will be using gravitational waveforms $h_{\ell m}$ extracted with the RWZ formalism [44–47]. The Appendix discusses details of the numerical implementation used to obtain $h_{\ell m}$ from the RWZ scalars, and presents a comprehensive comparison of the numerical $\Psi_4^{\ell m}$ and RWZ $h_{\ell m}$ waveforms. Consistency between the two wave-extraction schemes is good, with phase differences less than 0.02 radians for the (2, 2) mode until about a time $20M$ after the peak of $|h_{22}|$.

Because we have more experience with the NP scalars during the inspiral, and because Ψ_4^{22} appears to behave better than RWZ h_{22} during ringdown (see Fig. 14 in the Appendix), we prefer to use the numerical Ψ_4 data. Therefore, during the inspiral phase, we will calibrate the EOB-adjustable parameters by comparing the second time derivative of EOB h_{22} against the numerical Ψ_4^{22}. During the plunge-merger phase, when the time derivatives of the waveform vary most rapidly, it is more difficult to calibrate the EOB $\ddot{h}_{22}$ since the resummation techniques in the EOB model were aimed at providing us with the best h_{22}. Therefore, around the time of merger, we shall calibrate the EOB h_{22} to the RWZ h_{22}. Note also that data analysis is based on $h_{\ell m}$, further motivating our choice to build the best EOB model for $h_{\ell m}$. Nevertheless, after calibration, in Sec. III C, we show comparisons of the EOB waveforms with both the numerical RWZ h_{22} and Ψ_4^{22}. The ringdown part of the numerical waveform is not used in the calibration of the EOB parameters; the QNMs are determined solely from the mass and spin of the final hole.

A. Waveform alignment and uncertainties in numerical waveforms

As previous investigations [21,26,31,48,49] have shown, the phase error between two waveforms depends crucially on the procedure used to align them in time and phase. For the *inspiral phase*, we shall adopt here the alignment procedure introduced in Ref. [22] (see also Ref. [33]) that consists of minimizing the quantity

$$\Xi(\Delta t,\Delta\phi)=\int_{t_1}^{t_2}[\phi_1(t)-\phi_2(t-\Delta t)-\Delta\phi]^2dt, \quad (23)$$

over a time shift Δt and a phase shift $\Delta\phi$, where $\phi_1(t)$ and $\phi_2(t)$ are the phases of the two waveforms. This alignment procedure has the advantage of averaging over the numerical noise and residual eccentricity when aligning numerical and EOB waveforms. The range of integration (t_1, t_2) is chosen to be as early as possible, where we expect the PN-based EOB waveform to be most valid, but late enough so that it is not contaminated by the junk radiation present in the numerical initial data. Moreover, the range of integration should be large enough for the integral to average over noise and residual eccentricity. Here, we fix $t_1=1040M$ and $t_2=2260M$ (measured from the start of the numerical waveform), so that we include three full cycles of phase oscillations due to eccentricity.

Using this alignment procedure, we estimate the errors on the numerical Ψ_4^{22} by comparing Ψ_4^{22} computed at different numerical resolutions and/or using different extrapolation procedures. In particular, Fig. 1 summarizes the phase errors for a set of numerical Ψ_4^{22} computed in Ref. [23]. The numerical waveform labeled ''N6, $n=3$'' (identical to the run ''30c1/N6, $n=3$'' from [23]) is the reference numerical waveform used throughout this paper unless otherwise noted. This waveform is the most accurate waveform from Ref. [23], extracted at various radii and then extrapolated to infinity. The waveforms with different values of n vary the order of the extrapolation and are used to quantify the uncertainty in the phase due to extrapolation, while those labeled by N5 (as opposed to N6) are from a simulation with a lower numerical resolution and are used to quantify the uncertainty due to nu-

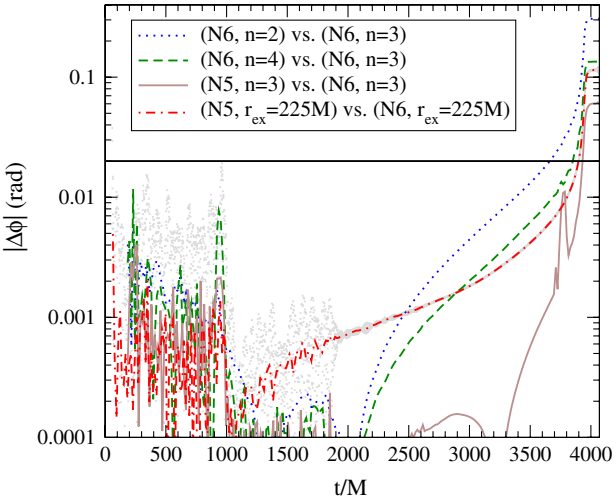

FIG. 1 (color online). Numerical error estimates. Phase difference between numerical Ψ_4^{22} waveforms, when aligned using the same procedure as employed for the EOB-NR alignment [see Eq. (23)]. "N6" and "N5" denote the highest- and next-to-highest numerical resolution, n denotes the order of extrapolation to infinite extraction radius, and "$r = 225M$" denotes waves extracted at finite radius $r = 225M$. The data are smoothed with a rectangular window of width $10M$; the light grey dots represent the unsmoothed data for the N5–N6 comparison at $r_{\rm ex} = 225M$.

merical truncation errors. Figure 1 also includes a comparison between waveforms extracted at finite coordinate radius $r_{\rm ex} = 225M$.

Extrapolation with $n = 2$ leads to systematic errors in the extrapolated waveform (see, Fig. 10 of Ref. [21]), which in turn results in a systematic error in Δt. Therefore, the blue dashed line in Fig. 1 represents a possibly overly conservative error estimate. The feature of the solid brown curve around $t \approx 3700M$ is due to an issue with data processing of the lower resolution "N5" run.

The primary use of Fig. 1 is to assess numerical errors relevant for the calibration of the EOB *inspiral* phase. By construction of the alignment procedure, this figure shows the numerical errors for waveforms that are aligned in the interval $[t_1, t_2]$, several orbits before merger. Calibrating the EOB inspiral phase in this manner is appropriate, because it ensures that early in the inspiral, the EOB model and the numerical simulation agree well, i.e., that we expect little dephasing at lower frequencies. This is important for waveform templates of low mass binaries, where the early inspiral waveform lies in LIGO's sensitive frequency band.

Figure 1 shows that the numerical Ψ_4^{22} waveforms are accurate to a few hundredths of a radian until very close to merger, when compared with our alignment procedure. Furthermore, Fig. 15 in the Appendix demonstrates that NP and RWZ waveforms differ by only 0.02 radians through inspiral and merger. Therefore, we shall adopt a deviation of 0.02 radians between EOB and NR inspiral waveforms as our goal for the EOB inspiral calibration. The horizontal line in Fig. 1 indicates this phase difference of 0.02 radians, and it will be our requirement when calibrating the EOB values of Ψ_4^{22}. The numerical phase errors exceed 0.02 radians at times $t = 3660M$, $3850M$, $3900M$, and $3933M$, respectively, and so our goal will be for EOB to agree to 0.02 radians at least up to $t \approx 3900M$. The choice of 0.02 radians is motivated by the goal of bringing the disagreement between the EOB and numerical phases *at least* to the level of the numerical error (see Fig. 15).

B. Tuning the adjustable parameters of the equal-mass effective-one-body dynamics

We divide the adjustable parameters into two groups and tune them separately in two steps. The first group of EOB-*dynamics* parameters includes $\{a_5(\nu), v_{\rm pole}(\nu), a_{\rm RR}^{\mathcal{F}_\Phi}(\nu), a_{\rm RR}^{\mathcal{F}_r}(\nu), A_8\}$. These parameters determine the inspiral and plunge dynamics of the EOB model and affect the merger-ringdown waveform only indirectly through the waveform's phase and frequency around the matching point. [We note that the inspiral phase is independent of the parameters $a_i^{h_{\ell m}}$, see Eq. (18).] These parameters are calibrated to the numerical NP Ψ_4^{22}. The second group of EOB-*waveform* parameters includes $\{a_i^{h_{\ell m}}, t_{\rm match}^{\ell m}$, and $\Delta t_{\rm match}^{\ell m}\}$, and affect only the plunge-merger-ringdown but not the inspiral EOB waveform. These parameters are calibrated to the numerical RWZ h_{22}. All the possible

TABLE I. Summary of *all possible* adjustable parameters of the EOB model considered in this paper. As we shall discuss in the main text, we will not need all of these parameters. In particular, we find that for the black-hole binary simulations investigated here, the choices $a_{\rm RR}^{\mathcal{F}_r}(\nu) = 0 = a_{\rm RR}^{\mathcal{F}_\Phi}(\nu)$, $A_8 = 0$, $t_{\rm match}^{\ell m}(\nu)$ at the peak of the EOB orbital frequency, allow the numerical and EOB values of the GW phase and amplitude to agree within numerical error. Furthermore, we find that for an equal-mass black-hole binary coalescence it is sufficient to set $a_5(\nu) = \nu\lambda_0$ [see Eq. (7) with $\lambda_1 = 0$] and calibrate λ_0, $v_{\rm pole}(1/4)$, $\Delta t_{\rm match}^{22}(1/4)$ and $a_i^{h_{22}}(1/4)$. For an equal-mass black-hole binary coalescence it is even possible to calibrate *only one* EOB-dynamics adjustable parameter, λ_0 [see Eq. (7)] and let $v_{\rm pole} \to \infty$. Finally, for an unequal-mass binary inspiral it is sufficient either to set $\lambda_1 = 0$, use the value of λ_0 from the equal-mass binary case, and calibrate $v_{\rm pole}(\nu)$; or alternatively to let $v_{\rm pole} \to \infty$ and calibrate both λ_0 and λ_1 in $a_5(\nu)$ [see Eq. (7)].

EOB-dynamics adjustable parameters	EOB-waveform adjustable parameters
$a_5(\nu)$	$t_{\rm match}^{\ell m}(\nu)$
$v_{\rm pole}(\nu)$	$\Delta t_{\rm match}^{\ell m}(\nu)$
$a_{\rm RR}^{\mathcal{F}_r}(\nu)$ or $a_{\rm RR}^{\mathcal{F}_\Phi}(\nu)$	$a_i^{h_{\ell m}}(\nu)$; $i = 1, \ldots 4$
A_8	

adjustable parameters of the EOB model employed in this paper are summarized in Table I. In the first step of our calibration procedure, we reduce the phase difference before merger by tuning the EOB-dynamics parameters. In the second step, we use these fixed values of the EOB-dynamics parameters, and tune the EOB-waveform parameters.

Among the EOB-dynamics parameters, $a_5(\nu)$ and $v_{\rm pole}(\nu)$ are the most important as they affect the entire quasicircular evolution of the inspiral. The two radiation-reaction parameters $a_{\rm RR}^{\mathcal{F}_\Phi}$ and $a_{\rm RR}^{\mathcal{F}_r}$ are introduced to adjust the dynamics of late inspiral when we expect that the quasicircular assumption is no longer valid. The p4PN parameter A_8 in the energy flux also influences the entire evolution, but we find that A_8 is strongly degenerate with $a_5(1/4)$ throughout the inspiral until a time $\sim 100M$ before merger. Based on these considerations, we shall tune $a_5(1/4)$ and $v_{\rm pole}$ first and consider $a_{\rm RR}^{\mathcal{F}_\Phi}(1/4)$, $a_{\rm RR}^{\mathcal{F}_r}(1/4)$ and A_8 only when exploring how to further improve the late evolution.

Therefore, in our first step, we set $a_{\rm RR}^{\mathcal{F}_\Phi}(1/4) = a_{\rm RR}^{\mathcal{F}_r}(1/4) = A_8 = 0$ and vary $a_5(1/4)$ and $v_{\rm pole}(1/4)$. Applying the alignment procedure presented at the beginning of Sec. III A, we shift each EOB Ψ_4^{22} in time and phase to agree with the reference numerical waveform at low frequency, and determine the time when the phase difference between the numerical and EOB Ψ_4^{22} waveforms becomes larger than 0.02 radians. We denote this reference time as $t_{\rm ref}$.

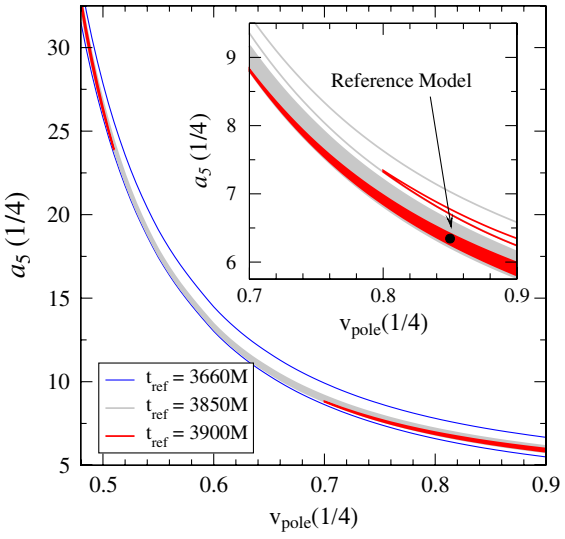

FIG. 2 (color online). In the parameter space of the EOB-dynamics adjustable parameters $a_5(1/4)$ and $v_{\rm pole}(1/4)$ we show the contours of the time $t_{\rm ref}$ at which the phase difference between the numerical "30c1/N6, $n = 3$" and EOB Ψ_4^{22} becomes larger than 0.02 radians. Note that the innermost red contours cover two disjoint regions. The inset shows the effect of numerical uncertainty: The filled contours are the $t_{\rm ref} = 3850M$ and $3900M$ contours from the main panel. The open contours are identical, except that they are computed using the "30c1/N6, $n = 2$" numerical Ψ_4^{22}. The reference model is shown as a black dot.

Figure 2 is a contour plot of the time $t_{\rm ref}$ in the $a_5(1/4) - v_{\rm pole}(1/4)$ parameter space. For all points inside the largest contours (blue curves), the associated EOB Ψ_4^{22} phase evolutions agree with the numerical ones up to $t = 3660M$, which is the earliest reference time considered in Sec. III A. In order to get EOB models that have phase differences less than 0.02 radians until $t = 3900M$, $a_5(1/4)$ and $v_{\rm pole}(1/4)$ have to be inside the innermost two separate thin contours (red curves). One might view these contours as encompassing all values of $a_5(1/4)$ and $v_{\rm pole}(1/4)$ that are consistent with the numerical inspiral waveform, given the fixed choices of the various other EOB parameters. There are $a_5(1/4)$ and $v_{\rm pole}(1/4)$ values that make the EOB phase differences less than 0.03 radians until $t = 3933M$, but not less than 0.02 radians until $t = 3933M$ (the latest reference time). We find that phase errors of the EOB Ψ_4^{22} corresponding to the upper left contours in Fig. 2 grow rapidly after $t = 3900M$, whereas phase errors of EOB Ψ_4^{22} corresponding to the lower-right contours grow only mildly until around $t = 3940M$. For this reason, we shall restrict the tuning of the other adjustable parameters to the lower-right region of Fig. 2 inside the innermost contour. As a reference set, we choose $a_5(1/4) = 6.344$ and $v_{\rm pole}(1/4) = 0.85$.[4] We note that the latter value is rather different from the value obtained in Ref. [31] when $a_5(1/4) = 6.25$ is used. This is due to differences between the EOB models—for example Ref. [31] employs the Padé-resummed GW energy flux with constant logarithms, whereas we use the Padé-resummed GW energy flux with factorized logarithms.

Quite interestingly, looking more closely at the red lines in the right corner of Fig. 2, as $v_{\rm pole}$ increases, we find another possible reference set $a_5(1/4) = 4.19$ and $v_{\rm pole} \to \infty$. With this choice, the pole in the Padé flux of Eq. (12) disappears.

In order to understand whether further tunings of radiation-reaction effects by adjusting the parameters $(v_{\rm pole}, a_{\rm RR}^{\mathcal{F}_\Phi}, a_{\rm RR}^{\mathcal{F}_r}, A_8)$ can modify the phasing during plunge, we compute how sensitive the phasing is to radiation-reaction effects once the binary has passed the last stable orbit (LSO) defined as $(\partial H^{\rm eff}/\partial r)_{\rm LSO} = 0 = (\partial^2 H^{\rm eff}/\partial r^2)_{\rm LSO}$. Reference [50] pointed out that the phas-

[4]We note that in Ref. [28], the authors suggested as best value $a_5(1/4) = 15$. However, the EOB model used in Ref. [28] differs from the one employed in this paper, the main difference being the GW energy flux. More importantly, the procedure used in Ref. [28] to calibrate $a_5(1/4)$ was different. It was based on maximized overlaps with white noise. The best value for $a_5(1/4)$ was obtained by requiring large overlaps, say ≥ 0.0975, for several mass ratios and (ℓ, m) modes (see Fig. 2 in Ref. [28]). Finally, the accuracy of the numerical waveforms employed in this paper differ from the ones in Ref. [28].

ing during the plunge is not affected much by radiation reaction, but driven mostly by the conservative dynamics. We want to quantify the latter statement more fully.

In order to do this, we need to define when the plunge starts. In the absence of radiation reaction, the plunge starts beyond the LSO where $r = r_{\rm LSO}$, $\omega = \omega_{\rm LSO}$, and $p_\Phi = p_\Phi^{\rm LSO}$. But in the presence of radiation reaction, Ref. [10] observed that there is not a unique $t_{\rm LSO}$ at which the conditions $r = r_{\rm LSO}$, $\omega = \omega_{\rm LSO}$ and $p_\Phi = p_\Phi^{\rm LSO}$ are satisfied. In fact, the above conditions may happen at different times (see Fig. 12 in Ref. [10]). Indeed, for the case $a_5(1/4) = 6.344$ and $\nu_{\rm pole}(1/4) = 0.85$, we find that with radiation reaction, $r(t^r_{\rm LSO}) = r_{\rm LSO}$, $\omega(t^\omega_{\rm LSO}) = \omega_{\rm LSO}$, and $p_\Phi(t^{p_\Phi}_{\rm LSO}) = p_\Phi^{\rm LSO}$, where $t^r_{\rm LSO} = 3914.50M$, $t^\omega_{\rm LSO} = 3919.83M$, and $t^{p\Phi}_{\rm LSO} = 3885.53M$, and where the orbital frequencies corresponding to the three different $t_{\rm LSO}$ values are $M\Omega = 0.975$, 0.106, and 0.074, respectively. Following Ref. [10], we will say that the plunge starts during the time interval spanned by the values of $t_{\rm LSO}$, which in this case is $t_{\rm LSO} \sim 34M$ before merger.

In Fig. 3, we show the phase difference between the numerical and EOB h_{22} as a function of the numerical GW frequency $M\omega_{22}$ for EOB models in which the GW energy flux is suddenly shut down at several EOB orbital frequencies. The cyan curve in Fig. 3 is obtained when the GW energy flux is not shut down. Note that in this case the phase difference increases fast close to the EOB matching point, which is marked by the vertical line in Fig. 3. The phase difference can change considerably its shape (including the sign of the slope close to the EOB matching point) when the energy flux is shut down before $M\Omega = 0.12$–0.13, but it does not change much, especially the fast increase close to the matching point, when the energy flux is shut down after $M\Omega = 0.12$–0.13, immediately after the LSO defined by the condition $\omega(t^\omega_{\rm LSO}) = \omega_{\rm LSO}$ above.

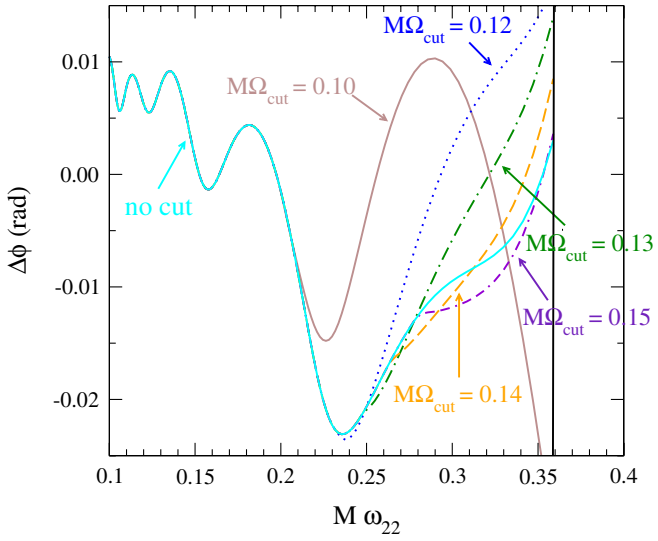

FIG. 3 (color online). For the case $a_5(1/4) = 6.344$ and $\nu_{\rm pole}(1/4) = 0.85$ ($A_8 = 0$, $a^{\mathcal{F}_\Phi}_{\rm RR} = 0$ and $a^{\mathcal{F}_r}_{\rm RR} = 0$), we show the phase difference between the numerical and EOB mode h_{22} versus the numerical GW frequency $M\omega_{22}$ for EOB models in which the GW energy flux is shut down at several EOB orbital frequencies. The vertical line marks the maximum EOB orbital frequency.

This study suggests that it is difficult to modify the behavior of the EOB phasing during plunge by tuning only the adjustable parameters entering the radiation-reaction terms or the GW energy flux, $a^{\mathcal{F}_r}_{\rm RR}(\nu)$, $a^{\mathcal{F}_\Phi}_{\rm RR}(\nu)$ and A_8, $\nu_{\rm pole}(\nu)$. The behavior of the EOB phasing during plunge is more sensitive to adjustable parameters in the EOB conservative dynamics, e.g., $a_5(\nu)$ at 4PN order or $a_6(\nu)$ at 5PN order, etc. However, the parameters $a_i(\nu)$ also affect the phasing during the very long inspiral, and a careful tuning is needed to reach excellent agreement both during inspiral and plunge.

Nevertheless, it is possible to modify the behavior of the EOB phasing during the late inspiral by tuning A_8, $a^{\mathcal{F}_r}_{\rm RR}(1/4)$ and $a^{\mathcal{F}_\Phi}_{\rm RR}(1/4)$ *together with* $a_5(1/4)$ and $\nu_{\rm pole}(1/4)$. As an example of this, we redo the contour plot shown in Fig. 2, but with $a^{\mathcal{F}_r}_{\rm RR}(1/4) = 0.5$ instead of zero. The result is shown as dashed curves in Fig. 4. We still find EOB models that have phase differences less than 0.02 radians until $t = 3900M$. In particular, with the reference value $\nu_{\rm pole}(1/4) = 0.85$ and choosing $a_5(1/4) = 6.013$, we find that the behavior of the EOB phasing is substantially modified only for the last $40M$ of evolution before merger. In this case, the change in phase difference is in the range of 0.01–0.1 radians, and the slope of phase difference at the matching point can change sign. Similar

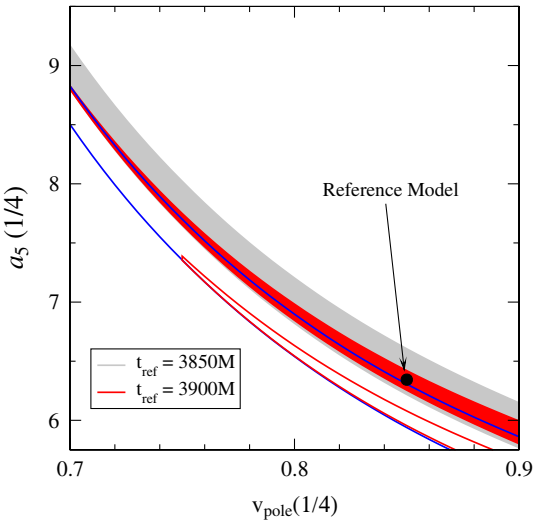

FIG. 4 (color online). Effect of $a^{\mathcal{F}_r}_{\rm RR}$ on contours of acceptable EOB parameters. The solid contours are the $t_{\rm ref} = 3850M$ and $3900M$ contours from Fig. 2. The open contours shifted to the lower-right are the same, but computed with $a^{\mathcal{F}_r}_{\rm RR} = 0.5$ instead of $a^{\mathcal{F}_\Phi}_{\rm RR} = 0$. The reference model is shown as a black dot.

results are obtained when repeating this analysis with $a_{\rm RR}^{\mathcal{F}_\Phi}(1/4)$ or A_8 different from zero. We also observe that the effect on the dynamics of the adjustable parameter $a_{\rm RR}^{\mathcal{F}_\Phi}(1/4)$ is almost equivalent to the effect of the adjustable parameter $a_{\rm RR}^{\mathcal{F}_r}(1/4)$, except for a minus sign and a different scaling. So it is not necessary to consider both of these radiation-reaction adjustable parameters.

Although time consuming, in principle it is possible to perform a comprehensive search over the complete set of the EOB-dynamics parameters $a_5(\nu)$, $\upsilon_{\rm pole}(\nu)$, A_8, $a_{\rm RR}^{\mathcal{F}_r}(\nu)$ or $a_{\rm RR}^{\mathcal{F}_\Phi}(\nu)$. However, at this point there is no need to further improve the EOB evolution close to merger, and achieve better agreement with the equal-mass, nonspinning numerical data, since the agreement is already at the level of the numerical error. Thus, in the following, we shall use the values of $a_5(1/4)$ and $\upsilon_{\rm pole}(1/4)$ based on Fig. 2, obtained by setting to zero all the other EOB-dynamics adjustable parameters in Table I. We will leave a comprehensive study of the other EOB-dynamics adjustable parameters to future work when highly accurate numerical merger waveforms of unequal-mass black-hole binaries become available.

We shall now discuss the EOB model with reference values $a_5(1/4) = 6.344$ and $\upsilon_{\rm pole}(1/4) = 0.85$, and tune the EOB-waveform adjustable parameters. We shall comment at the end of this section on the results when the other reference values $a_5(1/4) = 4.19$ and $\upsilon_{\rm pole}(1/4) \to \infty$ are used. In Fig. 5 we compare the numerical and EOB h_{22} amplitudes with and without including NQC terms. The agreement of the numerical amplitude with the EOB amplitude of Eq. (16a) without NQC terms, which uses the resummation procedure of Ref. [17], is rather remarkable. The relative difference at the peak is only $\sim$1.5%, and the EOB peak amplitude occurs only $\sim 6M$ before the numerical peak amplitude. We notice that this excellent agreement is due to the presence in ρ_{22} of test-particle corrections through 5PN order. Were the test-particle corrections through 4PN or 5PN orders not included, the disagreement at the peak would become 4.9% and 11.3%, respectively.[5]

Figure 5 also shows the EOB amplitudes of Eq. (16a) when the Padé resummations P_4^1 and P_3^2 of ρ_{22} suggested in Ref. [17] are applied. In these cases, the EOB peak amplitude almost coincides in time with the numerical peak amplitude, but the relative difference in the value of the peak amplitude is rather large. However, those large differences may be resolved if the resummed version of the

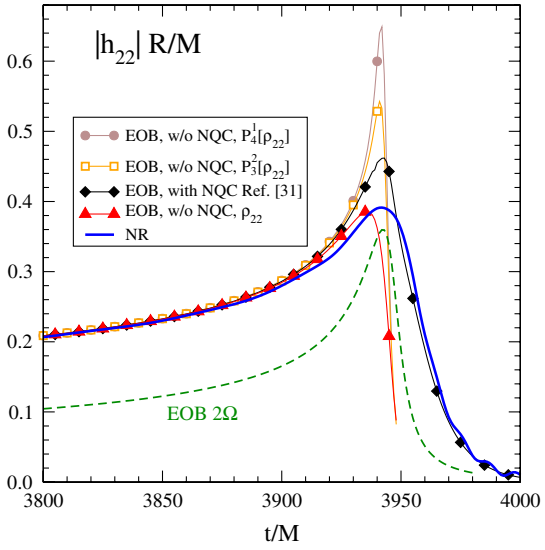

FIG. 5 (color online). We compare the numerical and EOB h_{22} amplitudes when the EOB model with reference values $a_5(1/4) = 6.344$ and $\upsilon_{\rm pole}(1/4) = 0.85$ are used. We show the EOB amplitudes without the NQC corrections and the EOB amplitude with the NQC terms suggested in Ref. [31], where the NQC parameters take the values $a = 0.75$ and $\epsilon = 0.09$. When the NQC corrections are not included, we show the EOB amplitude of Eq. (16a), which uses the resummation procedure of Ref. [17], and also the EOB amplitudes of Eq. (16a) when the Padé resummations P_4^1 and P_3^2 of ρ_{22} suggested in Ref. [17] are applied. Note that in this plot, the EOB amplitudes do not contain the merger-ringdown contribution.

GW energy flux [17] consistent with the resummed $h_{\ell m}$ were used. Figure 5 also contains the EOB h_{22} amplitude with NQC terms as suggested in Refs. [30,31] [see Eq. (12) in Ref. [31]]. The relative difference with the numerical amplitude is $\sim$20% at the peak. It is rather interesting to observe, as pointed out in Ref. [31], that by aligning the numerical and EOB waveforms at low frequency, we find that the peak of the numerical h_{22} coincides with the peak of the EOB orbital frequency. Here, to improve the amplitude agreement during plunge and merger, we include the NQC corrections of Eq. (18). We fix two of the adjustable parameters, $a_1^{h_{22}}$ and $a_2^{h_{22}}$, by requiring that a local extremum of the EOB h_{22} amplitude occurs at the same time as the peak of the EOB orbital frequency (i.e., the EOB light ring), and that the EOB amplitude at the peak coincides with the numerical amplitude at the peak. In fact, we expect that in the near future, the peak of the numerical h_{22} will be able to be predicted by numerical relativity with high accuracy for several mass ratios. Thus, the peak can be fit with a polynomial in ν. (Preliminary studies that use results from Ref. [28] confirm this expectation.) The other two adjustable parameters, i.e., $a_3^{h_{22}}$ and $a_4^{h_{22}}$, are calibrated to the numerical results to further reduce the disagreement. Specifically, we do a two-parameter least-square fit of the ratio of the numerical RWZ and EOB $h_{\ell m}$ on Eq. (18) in

[5]In Ref. [17] (see Fig. 10 therein and discussion around it) the authors pointed out that the difference between h_{22} amplitudes computed with the test-particle corrections through 3PN, 4PN, or 5PN orders, differ *only* by a few percent. However, this statement was obtained for circular orbits until the LSO frequency $M\Omega = 0.097$. Our Fig. 5 extends beyond that frequency (the latter corresponds to $t = 3914M$ in the figure).

which $a_1^{h_{22}}$ and $a_2^{h_2}$ are fixed as functions of $a_3^{h_{22}}$ and $a_4^{h_2}$ by the requirements described above. We notice that the strategy of improving the amplitude agreement followed in this paper might change in the future, when accurate numerical unequal-mass black-hole binary inspiral-merger-ringdown waveforms become available. A smaller number of adjustable parameters might suffice if more requirements on the EOB model itself can be imposed or if a different matching procedure, such as the one suggested in Ref. [51], is employed.

C. Comparing the gravitational-wave modes $h_{\ell m}$ of equal-mass *coalescing* black-hole binaries

In this section, we focus on the model whose EOB-dynamics and EOB-waveform adjustable parameters were calibrated to numerical RWZ h_{22} and NP Ψ_4^{22} in Sec. III B. Using this EOB model, we generate the GW modes h_{22}, h_{32}, and h_{44}, and compare them to the corresponding numerical modes. We choose these three modes because they are the most dominant ones for an equal-mass, nonspinning black-hole binary.

In Fig. 6, we show the numerical and EOB mode h_{22} aligned with the procedure of Sec. III A. Using the reference values $a_5(1/4) = 6.344$ and $v_{\rm pole}(1/4) = 0.85$, we find that the best phase and amplitude agreement is obtained when the matching occurs at an interval of $\Delta t^{22}_{\rm match} = 3.0M$ ended at $t^{22}_{\rm match} = 3942.5M$, i.e., at the peak of $M\Omega$, with $a_1^{h_{22}}(1/4) = -2.23$ and $a_2^{h_{22}}(1/4) = 31.93$, $a_3^{h_{22}}(1/4) = 3.66$ and $a_4^{h_{22}}(1/4) = -10.85$. The phase difference is strictly within ± 0.02 radians until the merger, i.e., the peak of h_{22}, which happens at $t = 3942.5M$ (early numerical data contaminated by junk radiation was discarded until $t = 200M$). The relative amplitude difference is also within ± 0.02 in this range. The phase difference becomes 0.04 radians at $t = 3962M$, before a rather large error starts contaminating the numerical h_{22}. A more careful tuning on the EOB-waveform adjustable parameters could further improve the phase agreement. However, we do not think it is worthwhile to improve the agreement at this point since we are only examining the equal-mass case. Note that the relative amplitude difference becomes $\sim 7\%$ at $t = 3962M$, and increases during the ringdown.

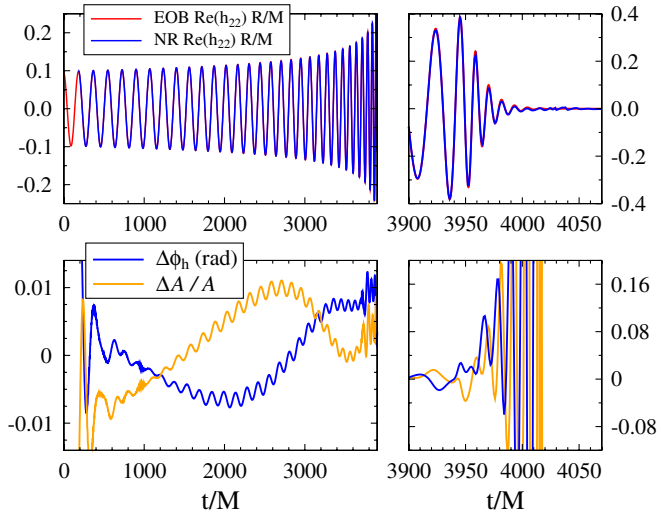

FIG. 6 (color online). Comparison of numerical waveform to EOB waveform with $a_5(1/4) = 6.344$ and $v_{\rm pole}(1/4) = 0.85$, i.e., the same model used in Fig. 5. The top panels show the real part of numerical and EOB h_{22}, the bottom panels show amplitude and phase differences between them. The left panels show times $t = 0$ to $3900M$, and the right panels show times $t = 3900$ to $t = 4070M$ on a different vertical scale.

The numerical GW strain h_{22} plotted in Fig. 6 is computed using RWZ wave extraction. During the ringdown, this waveform is noisier than the extracted NP scalar Ψ_4^{22} (see the Appendix). Therefore, in Fig. 7, we compare the numerically extracted Ψ_4^{22} with the second time derivative $\ddot{h}_{22}$ of the EOB waveform. Overall, the agreement is much better than for the comparison of h_{22} in Fig. 6. Phase and relative amplitude differences are smaller than 0.002 during most of the inspiral, and remain smaller than 0.01 up to

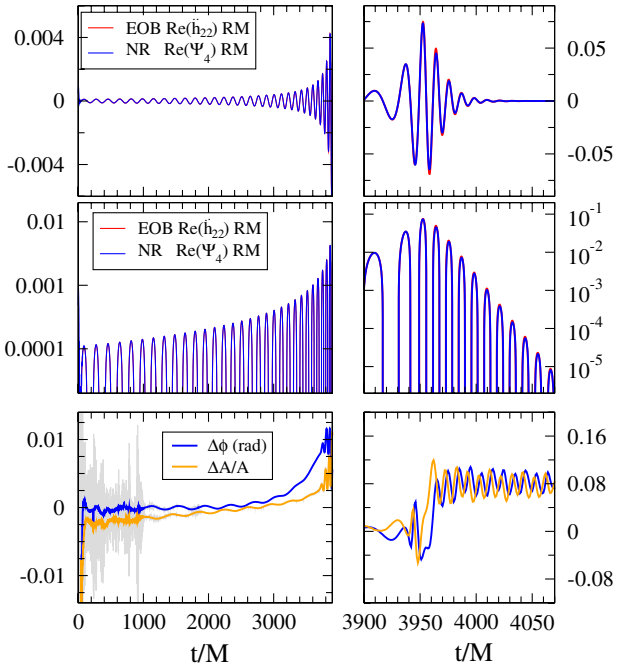

FIG. 7 (color online). Comparison between EOB $\ddot{h}_{22}$ and the numerical Ψ_4^{22}. The top four panels show the real part of the waveform, on a linear and logarithmic y axis. The bottom two panels show the phase difference (in radians) and the fractional amplitude difference between the two waveforms. The left panels show times $t = 0$ to $3900M$, and the right panels show times $t = 3900$ to $t = 4070M$ with different vertical scales. (The quantities in the lower left panel have been smoothed; the grey data in the background of that panel presents the raw data.) This figure uses the same EOB model as Figs. 5 and 6, namely $a_5(1/4) = 6.344$ and $v_{\rm pole}(1/4) = 0.85$.

$t = 3920M$. In the interval around merger, $t = 3930M$ to $3960M$, the agreement is slightly worse than in Fig. 6; the disagreement in this region is caused by the differences between the inspiral EOB $\ddot{h}_{22}$ and numerical NP Ψ_4^{22} frequencies, as discussed at the beginning of Sec. III.

In the ringdown region, $t > 3960M$, Fig. 7 shows excellent agreement, and this agreement persists until late times. In contrast to the h comparison shown in Fig. 6, in Fig. 7 both phase and amplitude differences remain *bounded*; during the ringdown, the phase difference between EOB $\ddot{h}_{22}$ and Ψ_4^{22} oscillates around 0.08 radians, and the amplitude differs by about 8%. Apart from small oscillations likely caused by gauge effects (see the Appendix), $\Delta\phi$ remains constant to an excellent degree during about 9 ringdown oscillations, i.e., during an accumulated phase of about 56 radians. If the quasinormal mode frequency used in the EOB ringdown waveform were different from the numerical ringdown frequency by as little as 0.1%, a linearly accumulating phase difference of $\sim$0.056 radians would accumulate, which would be clearly noticeable in the lower-right panel of Fig. 7. Thus, we find agreement at the 0.1% level between the numerical quasinormal mode frequency and the prediction based on final mass and spin of the numerical simulation.

In Fig. 8, we compare the amplitude and frequency of numerical and EOB h_{22} waveforms together with the orbital frequency of the EOB model. The peak of the latter is close to the EOB light ring, and is aligned with the maximum of both the EOB and numerical h_{22} amplitudes (as required by our choice of $a_1^{h_{22}}$ and $a_2^{h_{22}}$). During the ringdown, the frequency computed from the numerical h_{22} shows increasingly large oscillations. We also plot the frequency computed from the numerical Ψ_4^{22} mode. This frequency shows much smaller, and bounded, oscillations deep into the ringdown regime.

Having constructed our EOB waveform purely by considering the (2, 2) mode, we now discuss agreement between higher modes of the EOB model and the numerical simulation. Figure 9 shows phase and amplitude differences for the two next largest modes, the (4, 4) and the (3, 2) mode. The EOB model is identical to the one that has been calibrated to agree with the (2, 2) mode, and the parameters $a_i^{h_{32}}$ and $a_i^{h_{44}}$, which appear in Eq. (18) to correct the amplitude of the higher-order modes for nonquasicircular motion, are set to zero. But although the EOB model has not been calibrated in any way to match the higher-order modes, the agreement between numerical and EOB waveforms shown in Fig. 9 is rather good for $t \lesssim 3700M$. In fact, the differences between EOB and NR modes are comparable to the estimated numerical errors in these modes (as estimated by convergence tests between different numerical resolutions, and the comparison between the numerical h and Ψ_4 waveforms, which are presented in the Appendix). Around $t \approx 3700M$, the numerical (3, 2) and (4, 4) modes begin to show additional features, which we believe are unphysical, and are described in more detail in the Appendix. These features prevent a meaningful comparison of the (3, 2) and (4, 4) modes at later times.

Figure 10 shows amplitude and frequency of the (4, 4) and (3, 2) modes for both the EOB model and the numerical simulation for the last few hundred M of inspiral. This figure begins approximately where the NR-EOB differ-

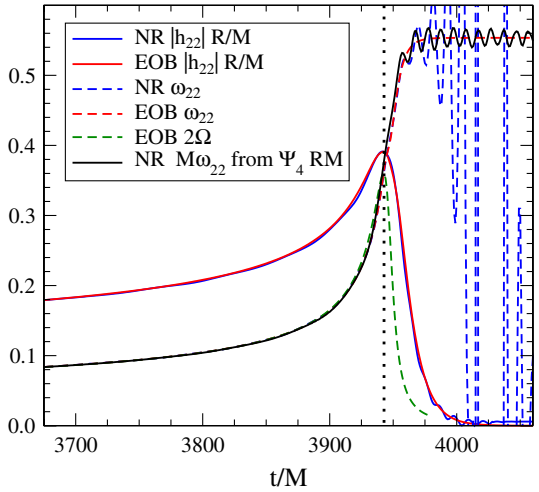

FIG. 8 (color online). We show the amplitude and frequency of the numerical and EOB mode h_{22}, the EOB orbital frequency and the frequency of the numerical mode Ψ_4^{22}. The vertical line marks the peak of the EOB amplitude and orbital frequency.

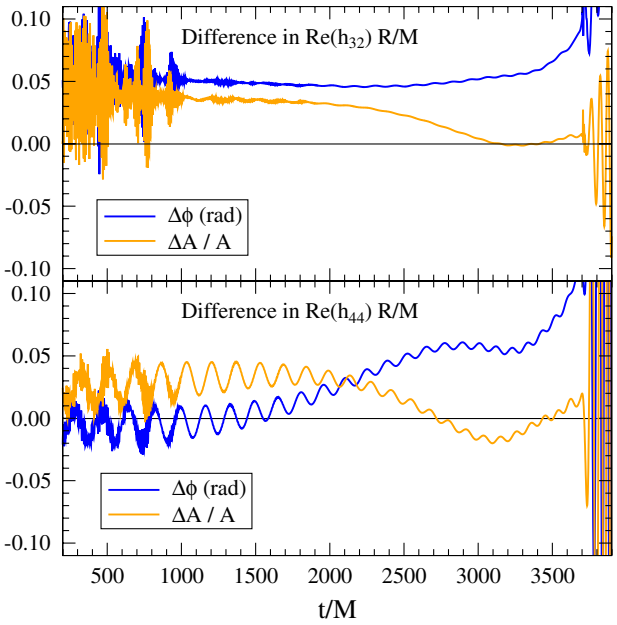

FIG. 9 (color online). Upper panel: Amplitude and phase differences of numerical and EOB mode h_{32} over the inspiral range. Lower panel: Amplitude and phase differences of numerical and EOB mode h_{44} over the inspiral range.

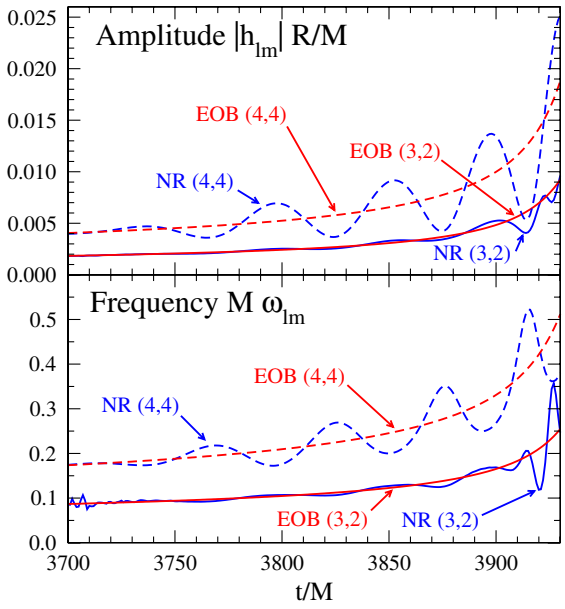

FIG. 10 (color online). Upper panel: Amplitude of the numerical and EOB modes h_{32} and h_{44}. Lower panel: Frequency of the numerical and EOB modes h_{32} and h_{44}. The EOB orbital frequency $2M\Omega$ ($4M\Omega$) is indistinguishable from the frequency of the h_{32} (h_{44}) mode on the scale of this plot.

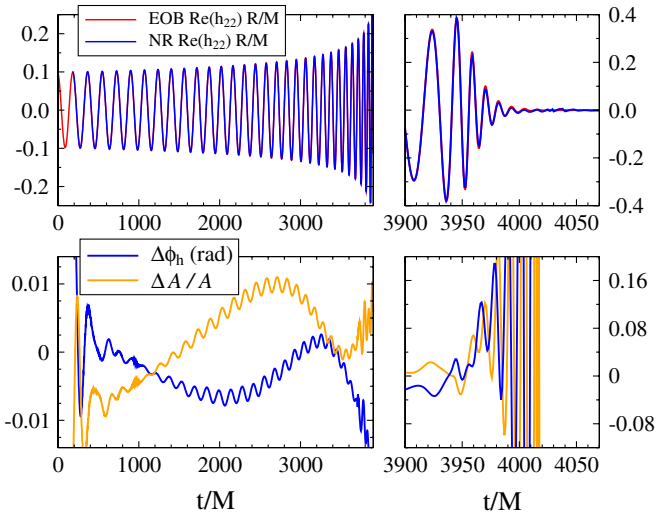

FIG. 11 (color online). Comparison of the numerical data to an EOB model with $v_{\rm pole} = \infty$. This figure is analogous to Fig. 6, but uses an EOB model that was calibrated with the restriction $v_{\rm pole} = \infty$ (parameters are given in the main text). Even without $v_{\rm pole}$, the inspiral can be matched equally well as in Fig. 6; during the ringdown, the phase differences are somewhat larger, but it is possible that refined tuning will reduce them further.

ences in Fig. 9 exceed the vertical scale of that figure. The EOB amplitude and phase follow roughly the average of numerical results, which show oscillations resulting from numerical errors. At earlier times, the EOB and NR amplitudes, phase and frequencies track each other very closely, as can be seen from Fig. 9. Please compare also with Fig. 8, which plots the frequencies for the (2, 2) mode.

Finally, in Fig. 11, we show the numerical and EOB mode h_{22} using the reference values $a_5(1/4) = 4.19$ and $v_{\rm pole} \to \infty$. In this case, we find that the best phase and amplitude agreement is obtained when the matching occurs over a range of $\Delta t^{22}_{\rm match} = 2.2M$ ended at the peak of $M\Omega$, with $a_1^{h_{22}}(1/4) = -2.50$ and $a_2^{h_{22}}(1/4) = 35.43$, $a_3^{h_{22}}(1/4) = 4.91$ and $a_4^{h_{22}}(1/4) = -32.40$. Comparing the result with that of Fig. 6, we notice that the phase and amplitude differences are only slightly worse than the reference model of Fig. 6, but still within numerical error.

D. Impact on data analysis

Using the EOB model with reference values $a_5(1/4) = 6.344$ and $v_{\rm pole}(1/4) = 0.85$, we now quantify the disagreement between numerical and EOB waveforms by calculating their maximized overlaps, which are important for analysis of data [52] from GW detectors. Here, we restrict ourselves to the dominant mode h_{22}. Given two time-domain waveforms $h_1(t)$ and $h_2(t; t_0, \phi_0)$ generated with the same binary parameters, the maximized overlap, otherwise known as a fitting factor (FF), is given explicitly by [27]

$$\mathrm{FF} \equiv \max_{t_0,\phi_0} \frac{\langle h_1, h_2(t_0, \phi_0)\rangle}{\sqrt{\langle h_1, h_1\rangle \langle h_2(t_0, \phi_0), h_2(t_0, \phi_0)\rangle}}, \tag{24}$$

where

$$\langle h_1, h_2\rangle \equiv 4\,\mathrm{Re}\int_0^\infty \frac{\tilde{h}_1(f)\tilde{h}_2^*(f)}{S_h(f)}\,df. \tag{25}$$

Here, $\tilde{h}_i(f)$ is the Fourier transform of $h_i(t)$, and $S_h(f)$ is the detector's power spectral density. We compute the FFs for binary black holes with total mass 30–150$M_\odot$, using LIGO, Enhanced LIGO, and Advanced LIGO noise curves,[6] and find in all cases FFs larger than 0.999. Note that the FFs are computed maximizing over time of arrival and initial phase, *but not* over the binary parameters. We note that FF ≥ 0.999 gives a mismatch $\epsilon \equiv 1 - \mathrm{FF}$ between the numerical and the analytical h_{22} of $\epsilon_{\rm NR\text{-}EOB} \leq 0.001$. For the noise curves of LIGO, Enhanced LIGO, and Advanced LIGO, we find that the mismatch between all extrapolated numerical waveforms h is less than 0.0001 for black-hole binaries with a total mass of 30–150$M_\odot$. If we take this mismatch as an estimate of the difference between the numerical and the *exact* physical waveforms, we have $\epsilon_{e-\rm NR} \leq 0.0001$. The mismatch between the exact and the analytical h_{22} is therefore $\epsilon_{e-\rm EOB} \leq 0.0017$. This mismatch is smaller than the bound 0.005 presented in

[6]For LIGO, we use the analytic fit to the LIGO design power spectral density given in Ref. [53]; and for Enhanced LIGO, we use the power spectral density given in [54] for Advanced LIGO, we use the broadband configuration power spectral density given at [55]

Ref. [8], and therefore our EOB model is sufficiently accurate for GW detection in LIGO, Enhanced LIGO, and Advanced LIGO.

E. Unequal mass *inspiraling* binary black holes

As a check of the robustness of our EOB model calibrated to numerical waveforms of equal-mass black-hole binaries, we extend the model to a set of unequal-mass black-hole binaries by comparing numerical and EOB Ψ_4^{22} inspiraling waveforms for mass ratios 2:1 and 3:1. These simulations were performed with the Caltech-Cornell SpEC code, last about eight orbits and have phase errors similar to the equal-mass simulation discussed so far. Details of these simulations will be published separately. We explore here the possibility of setting $a_5(\nu) = \nu\lambda_0$ with λ_0 constant and let $v_{\rm pole}$ depend on the mass ratio. Indeed, in the test-particle limit we expect[7] $1/\sqrt{3}$. $v_{\rm pole}(0) = 1/\sqrt{3} = 0.57\,735$, whereas in the equal-mass case we find $v_{\rm pole}(1/4) = 0.85$. As a preliminary study, we do not perform a comprehensive search over the $\lambda_0 - v_{\rm pole}$ parameter space for unequal-mass binaries, as we did for equal-mass binaries in Sec. III B. We fix λ_0 to our reference value 25.375 and tune $v_{\rm pole}(\nu)$ to require phase differences on the order of the numerical error.

In Figs. 12 and 13, we compare the numerical and EOB Ψ_4^{22} waveforms and their amplitude and phase differences for binaries with mass ratios $q = m_1{:}m_2$ of 2:1 and 3:1. The alignment procedure of Sec. III A was used with $t_1 = 310M$ and $t_2 = 930M$. The figures also show the numerical phase error obtained from runs with two different numerical resolutions. In the case of mass ratios $q = 2{:}1$ and 3:1, we find that by tuning $v_{\rm pole}(\nu)$, the difference between numerical and EOB waveforms can be reduced to values smaller than the numerical error. The best values of $v_{\rm pole}$ we find are $v_{\rm pole} = 0.76 \pm 0.01$ for mass ratio 2:1, and $v_{\rm pole} = 0.70 \pm 0.01$ for mass ratio 3:1. Choosing parameters outside this range results in differences between numerical and EOB waveforms that are at least twice the numerical error. Combining $v_{\rm pole}$ values for mass ratios 1:1, 1:2, 1:3, and the test-particle limit, we find a least-square fitting formula $v_{\rm pole}(\nu) = 0.57 - 0.65(\pm 0.35)\nu + 7.0(\pm 1.5)\nu^2$.

Finally, we observe that the phase and amplitude differences between numerical and EOB waveforms can be reduced to values smaller than the numerical error, if we choose the EOB reference model of Sec. III B, where we set $v_{\rm pole} \to \infty$ and let $a_5(\nu) = \nu(\lambda_0 + \lambda_1\nu)$. In particular, calibrating the mass ratio 2:1 and 3:1, we find $a_5(\nu) = \nu[-7.3(\pm 0.1) + 95.6(\pm 0.3)\nu]$. These EOB models agree

[7]We note that with our choice of the GW energy flux (factorized logarithms and $v_{\rm lso} = 1$), the best fit to numerical flux has $v_{\rm pole}(0) = 0.57$, which differs slightly from $1/\sqrt{3}$.

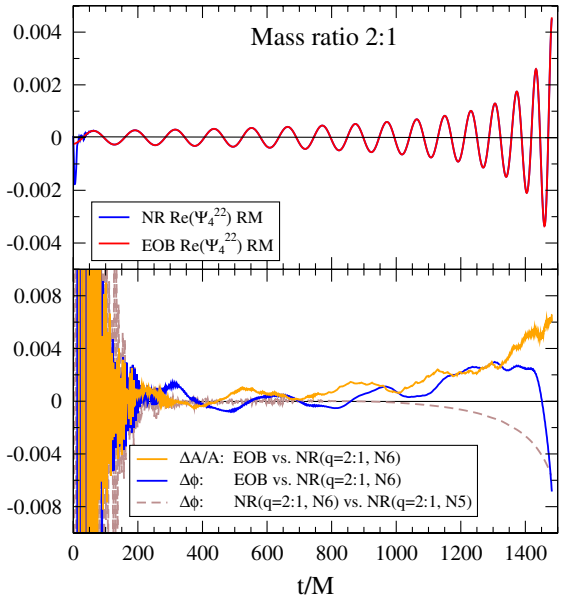

FIG. 12 (color online). EOB-NR comparison for a BH binary with mass ratio 2:1. The upper panel shows the numerical and EOB mode Ψ_4^{22}, and the lower panel shows phase and amplitude differences between EOB and numerical run. The dashed brown line is the estimated phase error of the numerical simulation, obtained as the difference between simulations at high resolution N6 and lower resolution N5.

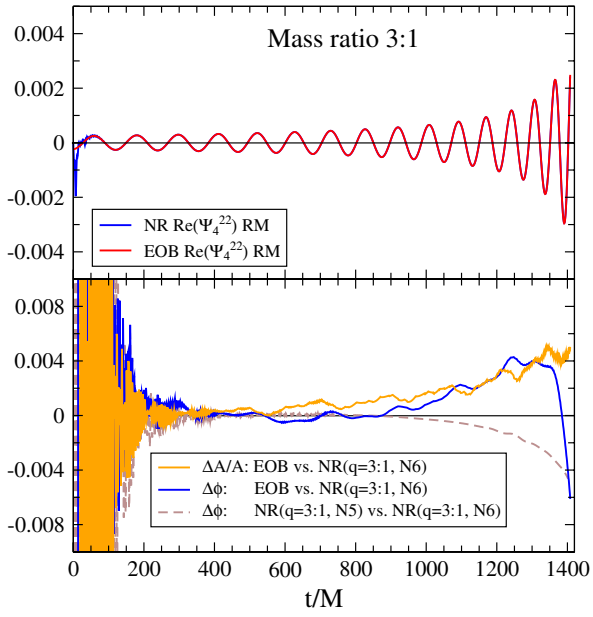

FIG. 13 (color online). EOB-NR comparison for a BH binary with mass ratio 3:1. The upper panel shows the numerical and EOB mode Ψ_4^{22}, and the lower panel shows phase and amplitude differences between EOB and numerical run. The dashed brown line is the estimated phase error of the numerical simulation, obtained as the difference between simulations at high resolution N6 and lower resolution N5.

with the numerical data as well as the EOB models shown in Figs. 12 and 13.

IV. CONCLUSIONS

In this paper, building upon recent, successful results [17,22,26–31] of the EOB formalism [9,10,13–15], we have concentrated on the EOB model denoted ${}^{\rm nK}F_4^4/H_4$ in Ref. [22], with adjustable EOB-dynamics and EOB-waveform parameters defined in Table I. We have calibrated this EOB model to a very accurate numerical simulation of an equal-mass nonspinning binary black-hole coalescence [23].

When comparing EOB and numerical waveforms, or when comparing numerical waveforms with each other, we determine the arbitrary time offset and phase offset between the waveforms by minimizing the phase differences between the waveforms over a time interval of $\sim 1000M$ at low frequency, where the PN-based EOB waveforms are expected to be most accurate [22]. Compared to aligning waveforms at a particular time or frequency, this procedure is less sensitive to numerical noise and residual eccentricity.

Among the EOB-dynamics adjustable parameters $\{a_5(1/4), v_{\rm pole}(1/4), a_{\rm RR}^{\mathcal{F}_\Phi}(1/4), a_{\rm RR}^{\mathcal{F}_r}(1/4), A_8\}$, the parameters $a_5(1/4)$ and $v_{\rm pole}(1/4)$ have the largest effect upon the long inspiral phase. Thus, we set $\{a_{\rm RR}^{\mathcal{F}_\Phi}(1/4) = 0, a_{\rm RR}^{\mathcal{F}_r}(1/4) = 0, A_8 = 0\}$ in our EOB model, and we considered the phase difference between the numerical and EOB Ψ_4^{22} as a function of the parameters $a_5(1/4)$ and $v_{\rm pole}(1/4)$. This phase difference increases with time, so we have sought parameters for which this phase difference remains small for as long a time as possible. We found regions of the $(a_5(1/4), v_{\rm pole}(1/4))$ parameter space where this phase difference is less than 0.02 radians either until $t = 282M$ or until $t = 42M$ before the time when the numerical h_{22} reaches its maximum amplitude (see filled contours in Fig. 2).

Moreover, building on Refs. [10,50], we have found that the EOB-dynamics adjustable parameters entering the GW energy flux cannot modify the phase of the EOB Ψ_4^{22} during the plunge and close to merger. This is because any modification of the GW energy flux beyond the LSO has negligible effect on the phasing, as the evolution is driven mostly by the conservative part of the dynamics. We also found that A_8 is strongly degenerate with $a_5(1/4)$ until almost $100M$ before merger, and that $a_{\rm RR}^{\mathcal{F}_r}(1/4)$ and $a_{\rm RR}^{\mathcal{F}_\Phi}(1/4)$ have an almost equivalent effect on the phasing, except for a minus sign and a different scaling. Overall, for the equal-mass nonspinning case, we have found that the EOB-adjustable parameters $\{a_{\rm RR}^{\mathcal{F}_\Phi}(1/4), a_{\rm RR}^{\mathcal{F}_r}(1/4), A_8\}$ have a minor effect in reducing the phase and amplitude differences between the EOB model and the numerical simulation (see also Fig. 4). To achieve differences on the order of the numerical error, we can restrict ourselves to the EOB parameter space with $\{a_{\rm RR}^{\mathcal{F}_\Phi}(1/4) = 0, a_{\rm RR}^{\mathcal{F}_r}(1/4) = 0, A_8 = 0\}$.

Furthermore, using our alignment procedure, we have found that the peak of the numerical h_{22} coincides with the peak of the EOB orbital frequency, confirming what was pointed out in Ref. [31]. As in Ref. [31], we require that the EOB dominant mode h_{22} peaks at the maximum of the EOB orbital frequency (i.e., the EOB light ring). We also require that the EOB amplitude at the peak coincides with the numerical amplitude at the peak. In fact, we expect that in the near future, the peak of the numerical h_{22} will be able to be predicted by numerical relativity with high accuracy for several mass ratios. Thus, the peak can be fit with a polynomial in ν. (Preliminary studies which use results from Ref. [28] confirm this expectation.) These requirements determine the EOB-waveform parameters $a_1^{h_{22}}(1/4)$ and $a_2^{h_{22}}(1/4)$. To further improve the agreement close to merger, we then tune $a_3^{h_{22}}(1/4)$, $a_4^{h_{22}}(1/4)$, and $\Delta t_{\rm match}^{22}(1/4)$, so that the phase and amplitude differences between the EOB and numerical h_{22} are minimized. In particular, we found that this happens if $\Delta t_{\rm match}^{22}(1/4)$ is chosen to be around $3M$ (while $t_{\rm match}^{22}(1/4)$ is fixed at the maximum of the EOB orbital frequency $M\Omega$). For the EOB reference model with $a_5(1/4) = 6.344$ and $v_{\rm pole} = 0.85$, we have found that the phase and amplitude differences between EOB and numerical h_{22} waveforms are 0.02 radians and 2%, respectively, until $20M$ before merger, and 0.04 radians and 7%, respectively, during merger and early ringdown, until the numerical h_{22} starts to be affected by numerical oscillations (see Fig. 6). These agreements were obtained by comparing EOB and numerical values of h_{22}, the latter having been extracted from the RWZ scalars. We also compared the EOB and numerical Ψ_4^{22}. In this case, the agreement is even better during the long inspiral and through the late ringdown, with phase and amplitude disagreements of 0.02 radians and 2% until $20M$ before merger, and 0.08 radians and 8%, respectively, during merger and ringdown (see Fig. 7). However, around the transition between plunge and ringdown, the EOB $\ddot{h}_{22}$ has some oscillations because the EOB resummation provides us with h_{22}, whereas when taking time derivatives of h_{22} nonresummed higher-order PN terms are generated, spoiling in part the agreement of $\ddot{h}_{22}$.

Quite interestingly, we have found that phase and amplitude differences between EOB and numerical waveforms can also be reduced to numerical errors, at least during the inspiral, if we let $v_{\rm pole} \to \infty$ and calibrate the coefficients λ_0 and λ_1 in $a_5(\nu) = \nu(\lambda_0 + \lambda_1\nu)$, see Fig. 11.

For data analysis purposes, we have also computed the maximized overlaps or FFs between the EOB reference model with $a_5(1/4) = 6.344$ and $v_{\rm pole} = 0.85$ and numerical h_{22}. We maximized only over the initial phase and time

of arrival. We have found that for black-hole binaries with total mass 30–150$M_\odot$, using LIGO, Enhanced LIGO, and Advanced LIGO noise curves, the FFs are larger than 0.999. We have also computed the FFs between values of numerical h_{22} that were computed in slightly different ways (e.g., different numerical resolutions, different extraction procedures), and have estimated the mismatch between the *exact* and EOB h_{22}. We have concluded, in the spirit of Ref. [8], that our analytical h_{22} satisfies the requirements of detection with LIGO, Enhanced LIGO, and Advanced LIGO.

Finally, to test the robustness of the EOB model, we have also compared it to a few equal-mass subdominant modes (ℓ, m), notably (4, 4) and (3, 2), and to the dominant mode (2, 2) of a set of unequal-mass inspiraling binaries. Without changing the EOB-dynamics adjustable parameters, we have found that, in the equal-mass case, the phase and amplitude differences of EOB and numerical h_{44} and h_{32} are within the numerical errors throughout the inspiral (see Figs. 9 and 10). Furthermore, in the unequal-mass case, we have found that we can reduce the phase difference of the EOB and numerical Ψ_4^{22} of inspiraling binaries of mass ratios 2:1 and 3:1 on the order of the numerical error (see Figs. 12 and 13). This can be obtained either (i) by setting $a_5(\nu) = \nu\lambda_0$ with λ_0 fixed by the equal-mass case, and calibrating $v_{\rm pole}(\nu)$, or (ii) by letting $v_{\rm pole} \to \infty$ and calibrating $a_5(\nu)$.

In the near future, we plan to compare the nonspinning EOB model defined in this paper to a larger set of accurate numerical simulations of black-hole binary coalescences (for both equal and unequal-mass binaries), and complete the tuning of all the EOB-dynamics and -waveform adjustable parameters. In particular, we expect to improve the EOB plunge-merger-ringdown matching either by reducing the number of EOB-waveform adjustable parameters or by employing different matching procedures or GW energy fluxes.

While polishing this manuscript for publication, an independent calibration of the EOB model, which uses the equal-mass binary black-hole data of the Caltech-Cornell Collaboration employed in this paper and made public on January 20, 2009, appeared on the archives [56].

ACKNOWLEDGMENTS

We thank O. Rinne for his work on implementing the Regge-Wheeler-Zerilli wave extraction, and F. Zhang for extrapolating waveforms to infinite extraction radius. We also thank E. Berti and E. Ochsner for useful discussions, and E. Berti for providing us with the quasinormal mode frequencies and decay times used in this paper. A. B. and Y. P. acknowledge support from NSF Grant No. PHY-0603762. L. B., L. K., H. P., and M. S. are supported in part by grants from the Sherman Fairchild Foundation to Caltech and Cornell, and from the Brinson Foundation to Caltech; by NSF Grants Nos. PHY-0601459, PHY-0652995, and DMS-0553302 at Caltech; by NSF Grants Nos. PHY-0652952 and DMS-0553677, and Grant No. PHY-0652929 at Cornell.

APPENDIX: COMPARING DIFFERENT METHODS OF COMPUTING $h_{\ell m}$

The analysis in Sec. III relies to some extent on the GW strain h extracted from the numerical simulation. Earlier papers describing generation of the numerical data [21–23] focused on the behavior of the NP scalar Ψ_4, and performed comparisons to PN theory based on the numerical Ψ_4.

We have two means of computing a GW strain h from the numerical simulations. The first is a double time integration of Ψ_4, exploiting the relation

$$\Psi_4 = \ddot{h}. \tag{A1}$$

[Note that throughout this Appendix, we suppress indices ℓm denoting the components of the decomposition into spin-weighted spherical harmonics. Thus, Eq. (A1) is meant to apply to each complex component (ℓ, m).] For each time integration [and each mode (ℓ, m)], a complex integration constant needs to be determined. These constants are fixed with the procedure described in Sec. II of Ref. [22], in which a certain functional of temporal variations of the amplitude of the integrated data is minimized. The minimization is performed over 25 separate integration intervals $[t_1, t_2]$ with $t_1/M = 1000, 1100, \ldots, 1400$ and $t_2/M = 2600, 2700, \ldots, 3000$. We then compute the time average of these 25 integrated waveforms, and we use this time average, which we denote as $\iint \Psi_4$, as the GW strain. Note that we perform the above operations on the numerical Ψ_4 data after it has been extrapolated to infinite extraction radius.

Our second means of extracting a GW strain is using the RWZ equations [44,45] generalized to arbitrary spherically symmetric coordinates, as formulated by Sarbach and Tiglio [46]. An advantage to the Sarbach and Tiglio formalism in contrast to the more widely used Zerilli-Moncrief formalism ([57] and references therein) is that in the former case, the GW strain is obtained directly from the gauge-invariant RWZ scalars (at leading order in the inverse radius), without any time integration. With Oliver Rinne, we have implemented the Sarbach and Tiglio formalism for a Minkowsi background in standard coordinates in the Caltech-Cornell spectral code [47]. From the RWZ scalars (extracted at finite radii), we compute the GW strain and then extrapolate to infinite extraction radius in order to obtain the final waveform $h_{\rm RWZ}$.

In order to gain insight into the accuracy and reliability of the computed GW strain, we explore the differences between waveforms extracted with either technique (see also [58] for a similar comparison). Figure 14 shows the real part of the numerical (2,2) mode. On the scale of the full waveform, no disagreement between $h_{\rm RWZ}$ and $\iint \Psi_4$

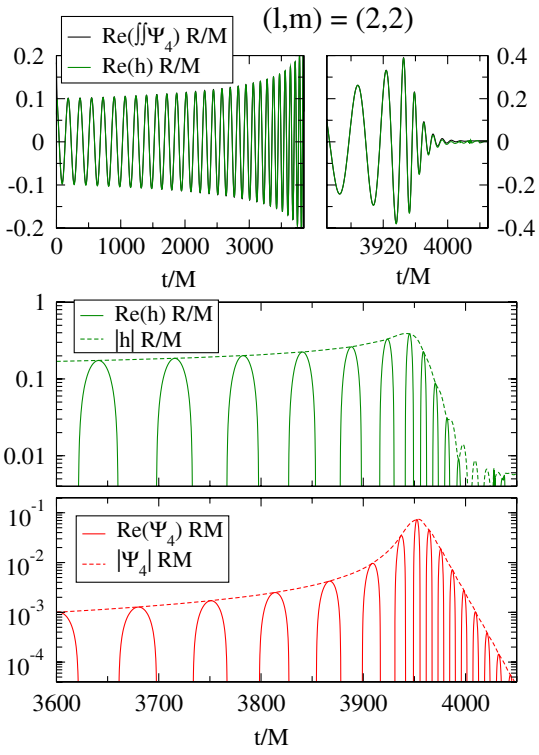

FIG. 14 (color online). The $(l, m) = (2, 2)$ mode of the numerical waveform.

is visible. However, the lower two panels of Fig. 14 show differences between h_{RWZ} and Ψ_4 deep in the ringdown phase: While Ψ_4 continues to decay exponentially through many orders of magnitude, h_{RWZ} exhibits noticeable deviation from a pure exponential decay at about a tenth of peak amplitude. Decay of h_{RWZ} stops completely at about 1% of peak amplitude.

We suspect that this unexpected behavior is caused by gauge effects: All simulations in the numerical relativity community are performed using gauges in which the coordinates dynamically respond to the changing geometry, so as to avoid pathologies such as coordinate singularities. Ideally, the procedures used to extract gravitational radiation from the simulations should be gauge invariant, so that the choice of gauge used in the simulation is irrelevant. In practice, however, wave-extraction techniques are not perfect. For example, the RWZ technique is gauge invariant only to first order in perturbation theory about fixed background coordinates. Likewise, the NP technique is strictly gauge invariant only if applied at future null infinity, rather than at a finite distance from the source. Gauge effects are expected to manifest themselves differently in NP and RWZ wave-extraction techniques, so by comparing the results of these two extraction techniques, we can get a handle on the size of our uncertainties that arise from gauge effects.

Therefore, we will examine the differences between the numerical h_{RWZ} and Ψ_4. Using (A1), we can compute a meaningful difference in two ways. The first way is to differentiate h_{RWZ} twice and compute

$$\Delta\phi_{\mathrm{NP}} = \arg(\Psi_4) - \arg(\ddot{h}_{\mathrm{RWZ}}), \tag{A2}$$

$$\frac{\Delta A_{\mathrm{NP}}}{A} = \frac{|\Psi_4| - |\ddot{h}_{\mathrm{RWZ}}|}{(|\ddot{h}_{\mathrm{RWZ}}| + |\Psi_4|)/2}. \tag{A3}$$

The subscript "'NP" indicates that the comparison is made on the level of the NP scalars, i.e., Ψ_4 appears undifferentiated on the right-hand sides. The second way is to time integrate Ψ_4 and to calculate

$$\Delta\phi_{\mathrm{RWZ}} = \arg\left(\iint \Psi_4\right) - \arg(h_{\mathrm{RWZ}}), \tag{A4}$$

$$\frac{\Delta A_{\mathrm{RWZ}}}{A} = \frac{|\iint\Psi_4| - |h_{\mathrm{RWZ}}|}{(|h_{\mathrm{RWZ}}| + |\iint\Psi_4|)/2}. \tag{A5}$$

The results of these comparisons are presented in Fig. 15. An examination of this figure reveals several properties of the extracted Ψ_4 and h_{RWZ} waveforms. First, we note that during the inspiral and merger (up to $t \lesssim 3960M$, that is $18M$ after the peak of h_{RWZ}), the RWZ and NP waveforms agree to better than 0.02 radians. $\Delta\phi_{\mathrm{NP}}$ contains more noise because noise is amplified by the double time differentiation to compute $\ddot{h}$, and because Ψ_4 is contaminated by junk radiation from the initial data up to time $t \approx 1000M$. The solid blue lines in this plot have been smoothed (by convolution with a Gaussian of width $5M$) to reduce the effect of noise due to junk radiation. (The grey data in the

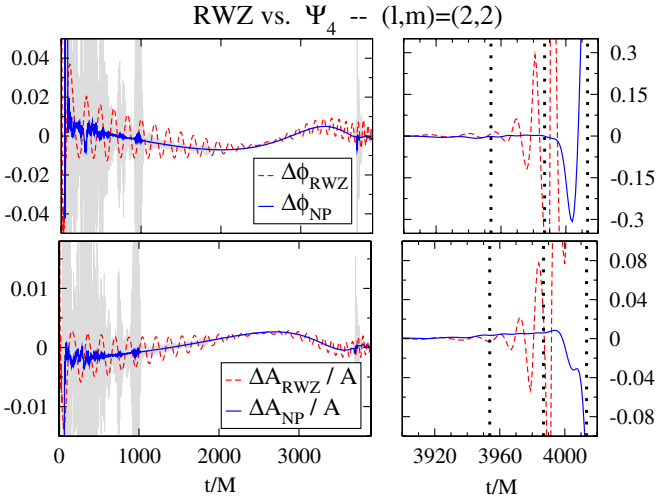

FIG. 15 (color online). Phase and relative amplitude difference between the $(l, m) = (2, 2)$ modes of the RWZ waveform h_{RWZ} and NP scalar Ψ_4 [see Eqs. (A2)–(A5)]. The right panel shows an enlargement of merger and ringdown, with the dotted vertical lines indicating time of maximum of $|\Psi_4|$, and where $|\Psi_4|$ has decayed to 10% and 1% of the maximal value. (The solid blue lines are smoothed; the grey data in the background represents the unsmoothed data.)

background of Fig. 15 shows the unsmoothed $\Delta\Phi_{\rm NP}$). In contrast, $\Delta\phi_{\rm RWZ}$ does not show similar high frequency noise (the red dashed curves in Fig. 15 are not smoothed). Integration naturally smooths noise and apparently, the RWZ wave extraction is less susceptible to the noise introduced by junk radiation. Unfortunately, because of an imperfect choice of integration constants for the time integration, $\iint\Psi_4$ does not precisely oscillate around zero at all times. This results in oscillations of $\Delta\phi_{\rm RWZ}$ and $\Delta A_{\rm RWZ}/A$ during the inspiral; the frequency of these oscillations coincides with the GW frequency. The choice of integration constants, however, is good enough to confine these oscillations to less than about 0.02 radians in phase and 0.5% in amplitude during the inspiral.

Around merger, differences of the wave strain, i.e., $\Delta\phi_{\rm RWZ}$ and $\Delta A_{\rm RWZ}/A$, begin to grow, and during ringdown this growth accelerates. This large disagreement is caused by two effects. The first effect is the contamination of $h_{\rm RWZ}$ in the ringdown phase, presumably by gauge effects, as shown in Fig. 14. The second effect is related to the time integration used to obtain $\iint\Psi_4$. During the inspiral phase, with an appropriate choice of integration constants the average value of $\iint\Psi_4$ is very nearly zero (see top left panel of Fig. 15). Thus, the inspiral phase fixes all integration constants. When we now extend the integration through merger and ringdown, we find that $\iint\Psi_4$ during ringdown has a contribution that grows linearly in time. Because the desired oscillatory part of $\iint\Psi_4$ decays exponentially, this linearly growing contribution contaminates $\arg\iint\Psi_4$ to an increasing degree as time increases. The linearly growing contribution to $\iint\Psi_4$ is just barely visible in the top panel of Fig. 14; for the (3,2) and (4,4) modes discussed below, it will be much more obvious.

When matching an analytical model waveform to numerical results, one must choose whether to match to Ψ_4, $\iint\Psi_4$, or $h_{\rm RWZ}$, and we have just seen that these three numerical waveforms differ by systematic effects that arise from properties of the numerical simulation. Given Figs. 14 and 15, it appears that Ψ_4 is preferable over $\iint\Psi_4$ because Ψ_4 lacks the low-frequency oscillations during inspiral that are introduced in $\iint\Psi_4$ by time integration, and furthermore Ψ_4 lacks the linear drift during the ringdown. Similarly, Ψ_4 has an advantage over $h_{\rm RWZ}$ because it has much cleaner behavior during ringdown (see Fig. 14).

We now turn our attention to the next largest mode, $(l, m) = (4, 4)$, which is shown in Fig. 16. Concentrating on the top panel first, we see that $\iint\Psi_4$ agrees with $h_{\rm RWZ}$ very well for a large fraction of the inspiral. However, for $t \lesssim 1000M$ and $t \gtrsim 3900M$, $\iint\Psi_4$ contains contributions that grow linearly in time. Note that these contributions cannot be removed by a different choice of integration constants, because integration constants result in addition of a linear term $a + bt$ *uniformly* at all times. Hence, if the integration constants were changed to yield agreement for

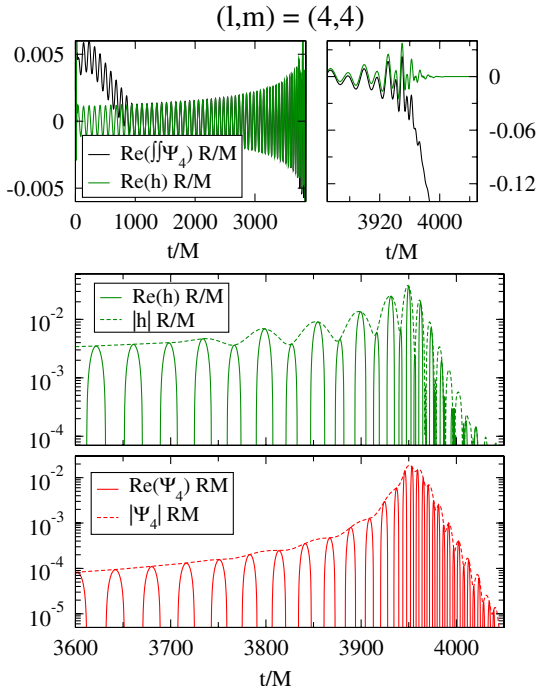

FIG. 16 (color online). The $(l, m) = (4, 4)$ mode of the numerical waveform.

$t \lesssim 1000M$, the linearly growing discrepancy would appear at $t \gtrsim 1000M$. The reason that the transition is around $t \sim 1000M$ may be related to the so-called junk radiation that is present in numerical simulations, and arises because the initial data do not correspond precisely to a snapshot of an evolution. A small fraction of the outgoing junk radiation is reflected when passing through the outer boundary. The reflected waves pass through the computational do-

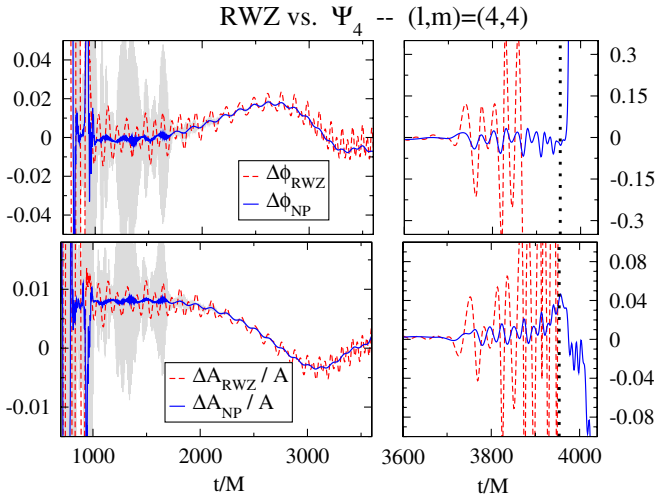

FIG. 17 (color online). Phase and relative amplitude difference between the $(l, m) = (4, 4)$ modes of the RWZ waveform $h_{\rm RWZ}$ and NP scalar Ψ_4, cf. Eqs (A2)–(A5). The right panels show an enlargement of merger and ringdown, with the dotted vertical line indicating the position of the maximum of $|\Psi_4|$.

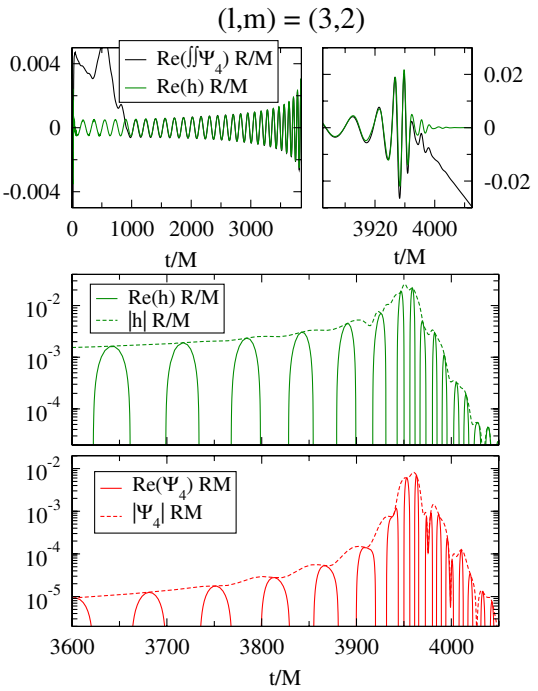

FIG. 18 (color online). The $(l, m) = (3, 2)$ mode of the numerical waveform.

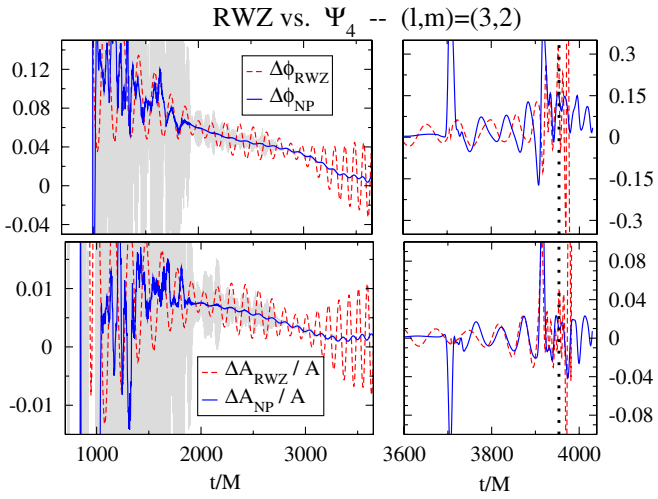

FIG. 19 (color online). Phase difference between the $(l, m) = (3, 2)$ modes of the RWZ waveform h and NP scalar Ψ_4, cf. Eqs (A2)–(A5). The right panels show an enlargement of merger and ringdown, with the dotted vertical line indicating the position of the maximum of $|\Psi_4|$.

main at retarded time $t \approx 1000M$. While the reflected junk radiation is small, apparently it is sufficient to contaminate $\iint \Psi_4$, as seen in the top left panel of Fig. 16.

Around merger, $t \approx 3950M$, $\iint \Psi_4$ picks up another linearly growing contribution, which renders $\iint \Psi_4$ basically useless during merger and ringdown. This contamination might be related to oscillations in Ψ_4 and h_{RWZ} that become visible at $t \gtrsim 3750M$ (see middle and lower panel of Fig. 16). It is presently unclear what causes these effects, but we conjecture that they are related to gauge effects that influence either our current wave-extraction procedure, or our current wave-extrapolation procedure. It is quite possible that a refined understanding of gauge effects will reduce these features in the future.

Because of the apparent contamination of the waveforms for early and late times, we restrict the EOB-NR comparison of the higher-order modes to the time interval $1000 \lesssim t/M \lesssim 3600$. Figure 17 shows that within this interval, Ψ_4 and h_{RWZ} agree to better than 0.02 radians in phase and 1% in amplitude.

Finally, Figs. 18 and 19 present an analogous comparison for the $(l, m) = (3, 2)$ mode. Qualitatively, these figures are similar to Figs. 16 and 17. Agreement between Ψ_4 and h_{RWZ} is very good for the time interval $1000 \lesssim t/M \lesssim 3700$, with the phases differing by less than 0.1 radians and the amplitudes by less than about 1%. The larger disagreement might be due to the smaller amplitude of the (3, 2) mode of Ψ_4 during the inspiral phase relative to the (4, 4) mode. One potentially interesting difference between the (4, 4) and (3, 2) modes lies in the relative size of the variations in $|h_{\mathrm{RWZ}}|$ and $|\Psi_4|$ in the time range $3700 \lesssim t/M \lesssim 3900$: For the (4, 4) mode, variations in $|\Psi_4|$ are clearly smaller than variations in $|h_{\mathrm{RWZ}}|$ (see Fig. 16). For the (3, 2) mode this is reversed, with $|h_{\mathrm{RWZ}}|$ showing somewhat smaller variations than $|\Psi_4|$.

[1] B. C. Barish and R. Weiss, Phys. Today **52**, 44 (1999).
[2] S. J. Waldman (LIGO Scientific Collaboration), Classical Quantum Gravity **23**, S653 (2006).
[3] S. Hild (LIGO Scientific Collaboration), Classical Quantum Gravity **23**, S643 (2006).
[4] F. Acernese, P. Amico, M. Alshourbagy, F. Antonucci, S. Aoudia, S. Avino, D. Babusci, G. Ballardin, F. Barone, L. Barsotti *et al.*, Classical Quantum Gravity **23**, S635 (2006).
[5] P. Fritschel, Proc. SPIE-Int. Soc. Opt. Eng.**4856** 282 (2003).
[6] L. S. Finn, Phys. Rev. D **46**, 5236 (1992).
[7] L. S. Finn and D. F. Chernoff, Phys. Rev. D **47**, 2198 (1993).
[8] L. Lindblom, B. J. Owen, and D. A. Brown, Phys. Rev. D **78**, 124020 (2008).
[9] A. Buonanno and T. Damour, Phys. Rev. D **59**, 084006 (1999).

[10] A. Buonanno and T. Damour, Phys. Rev. D **62**, 064015 (2000).
[11] L. Blanchet, Living Rev. Relativity **9**, 4 (2006).
[12] T. Damour, B. R. Iyer, and B. S. Sathyaprakash, Phys. Rev. D **57**, 885 (1998).
[13] T. Damour, P. Jaranowski, and G. Schäfer, Phys. Rev. D **62**, 084011 (2000).
[14] T. Damour, Phys. Rev. D **64**, 124013 (2001).
[15] T. Damour, B.R. Iyer, P. Jaranowski, and B.S. Sathyaprakash, Phys. Rev. D **67**, 064028 (2003).
[16] T. Damour and A. Nagar, Phys. Rev. D **76**, 064028 (2007).
[17] T. Damour, B. R. Iyer, and A. Nagar, arXiv:0811.2069.
[18] B. Brügmann, J. A. González, M. Hannam, S. Husa, U. Sperhake, and W. Tichy, Phys. Rev. D **77**, 024027 (2008).
[19] S. Husa, J. A. González, M. Hannam, B. Brügmann, and U. Sperhake, Classical Quantum Gravity **25**, 105006 (2008).
[20] M. Hannam, S. Husa, J. A. González, U. Sperhake, and B. Brügmann, Phys. Rev. D **77**, 044020 (2008).
[21] M. Boyle, D. A. Brown, L. E. Kidder, A. H. Mroué, H. P. Pfeiffer, M. A. Scheel, G. B. Cook, and S. A. Teukolsky, Phys. Rev. D **76**, 124038 (2007).
[22] M. Boyle, A. Buonanno, L. E. Kidder, A. H. Mroué, Y. Pan, H. P. Pfeiffer, and M. A. Scheel, Phys. Rev. D **78**, 104020 (2008).
[23] M. A. Scheel, M. Boyle, T. Chu, L. E. Kidder, K. D. Matthews, and H. P. Pfeiffer, Phys. Rev. D **79**, 024003 (2009).
[24] B. Vaishnav, I. Hinder, F. Herrmann, and D. Shoemaker, Phys. Rev. D **76**, 084020 (2007).
[25] M. Hannam *et al.*, arXiv:0901.2437.
[26] A. Buonanno, G. B. Cook, and F. Pretorius, Phys. Rev. D **75**, 124018 (2007).
[27] Y. Pan, A. Buonanno, J. G. Baker, J. Centrella, B. J. Kelly, S. T. McWilliams, F. Pretorius, and J. R. van Meter, Phys. Rev. D **77**, 024014 (2008).
[28] A. Buonanno, Y. Pan, J. G. Baker, J. Centrella, B. J. Kelly, S. T. McWilliams, and J. R. van Meter, Phys. Rev. D **76**, 104049 (2007).
[29] T. Damour and A. Nagar, Phys. Rev. D **77**, 024043 (2008).
[30] T. Damour, A. Nagar, E. N. Dorband, D. Pollney, and L. Rezzolla, Phys. Rev. D **77**, 084017 (2008).
[31] T. Damour, A. Nagar, M. Hannam, S. Husa, and B. Brügmann, Phys. Rev. D **78**, 044039 (2008).
[32] P. Ajith *et al.*, Classical Quantum Gravity **24**, S689 (2007).
[33] P. Ajith *et al.*, Phys. Rev. D **77**, 104017 (2008).
[34] T. Damour and A. Nagar, Phys. Rev. D **76**, 044003 (2007).
[35] T. Damour and A. Gopakumar, Phys. Rev. D **73**, 124006 (2006).
[36] H. Tagoshi and M. Sasaki, Prog. Theor. Phys. **92**, 745 (1994).
[37] L. E. Kidder, Phys. Rev. D **77**, 044016 (2008).
[38] L. Blanchet, G. Faye, B. R. Iyer, and S. Sinha, Classical Quantum Gravity **25**, 165003 (2008).
[39] E. Berti, V. Cardoso, and C. M. Will, Phys. Rev. D **73**, 064030 (2006).
[40] E. Berti, V. Cardoso, J. A. Gonzalez, U. Sperhake, M. Hannam, S. Husa, and B. Brügmann, Phys. Rev. D **76**, 064034 (2007).
[41] L. Rezzolla, E. Barausse, E. N. Dorband, D. Pollney, C. Reisswig, J. Seiler, and S. Husa, Phys. Rev. D **78**, 044002 (2008).
[42] J. D. Schnittman, A. Buonanno, J. R. van Meter, J. G. Baker, W. D. Boggs, J. Centrella, B. J. Kelly, and S. T. McWilliams, Phys. Rev. D **77**, 044031 (2008).
[43] E. Berti, V. Cardoso, K. D. Kokkotas, and H. Onozawa, Phys. Rev. D **68**, 124018 (2003).
[44] T. Regge and J. A. Wheeler, Phys. Rev. **108**, 1063 (1957).
[45] F. J. Zerilli, Phys. Rev. Lett. **24**, 737 (1970).
[46] O. Sarbach and M. Tiglio, Phys. Rev. D **64**, 084016 (2001).
[47] O. Rinne, L. T. Buchman, M. A. Scheel, and H. P. Pfeiffer, Classical Quantum Gravity **26**, 075009 (2009).
[48] J. G. Baker, J. R. van Meter, S. T. McWilliams, J. Centrella, and B. J. Kelly, Phys. Rev. Lett. **99**, 181101 (2007).
[49] J. G. Baker, S. T. McWilliams, J. R. van Meter, J. Centrella, D.-I. Choi, B. J. Kelly, and M. Koppitz, Phys. Rev. D **75**, 124024 (2007).
[50] A. Buonanno and T. Damour, in *The Ninth Marcel Grossmann Meeting*, edited by V. G. Gurzadyan, R. T. Jantzen, and R. Ruffini (World Scientific, Singapore, 2002), p. 1637.
[51] J. G. Baker, W. D. Boggs, J. Centrella, B. J. Kelly, S. T. McWilliams, and J. R. van Meter, Phys. Rev. D **78**, 044046 (2008).
[52] B. Aylott *et al.*, arXiv:0901.4399.
[53] T. Damour, B. R. Iyer, and B. S. Sathyaprakash, Phys. Rev. D **63**, 044023 (2001).
[54] http://www.ligo.caltech.edu/~rana/NoiseData/S6/DCnoise.txt.
[55] http://www.ligo.caltech.edu/advLIGO/scripts/ref_des.shtml.
[56] T. Damour and A. Nagar, Phys. Rev. D **79**, 081503 (2009).
[57] A. Nagar and L. Rezzolla, Classical Quantum Gravity **22**, R167 (2005).
[58] D. Pollney *et al.*, Phys. Rev. D **76**, 124002 (2007).